LM-00K80
September 17, 2000

Organized Oscillations of Initially-Turbulent Flow Past a Cavity

J.C. Lin, D. Rockwell

NOTICE

This report was prepared as an account of work sponsored by the United States Government. Neither the United States, nor the United States Department of Energy, nor any of their employees, nor any of their contractors, subcontractors, or their employees, makes any warranty, express or implied, or assumes any legal liability or responsibility for the accuracy, completeness or usefulness of any information, apparatus, product or process disclosed, or represents that its use would not infringe privately owned rights.

P	=	instantaneous pressure
ω	=	vorticity
u	=	streamwise (x) component of instantaneous velocity
u'	=	velocity fluctuation in x direction
v	=	transverse (y)
v'	=	velocity fluctuation in y direction
x,y	=	coordinates
t	=	time
β	=	fundamental of most unstable frequency of cavity shear layer
$\beta/2$	=	subharmonic of most unstable frequency of cavity shear layer
δ	=	boundary layer thickness
$( )_{rms}$	=	root-mean-square
$\overline{( )}$	=	time-averaged

I. Introduction

Flow past an open cavity is known to give rise to self-sustained oscillations in a wide variety of configurations, including slotted-wall, wind and water tunnels, slotted flumes, bellows-type pipe geometries, high-head gates and gate slots, aircraft components and internal piping systems. These cavity-type oscillations are the origin of coherent and broadband sources of noise and, if the structure is sufficiently flexible, flow-induced vibration as well. Moreover, depending upon the state of the cavity oscillation, substantial alterations of the mean drag may be induced. In the following, the state of knowledge of flow past cavities, based primarily on laminar inflow conditions, is described within a framework based on the flow physics. Then, the major unresolved issues for this class of flows will be delineated.

Self-excited cavity oscillations have generic features, which are assessed in detail in the reviews of Rockwell and Naudascher[1,2], Rockwell[3], Howe[4] and Rockwell[5]. These features, which are illustrated in the schematic of Figure 1, are: (i) interaction of a vorticity concentration(s) with the downstream corner; (ii) upstream influence from this corner interaction to the sensitive region of the shear layer formed from the upstream corner of the cavity; (iii) conversion of the upstream

influence arriving at this location to a fluctuation in the separating shear layer; and (iv) amplification of this fluctuation in the shear layer as it develops in the streamwise direction. In view of the fact that inflow shear-layer in the present investigation is fully turbulent, item (iv) is of particular interest. It is generally recognized, at least for laminar conditions at separation from the leading-corner of the cavity, that the disturbance growth in the shear layer can be described using concepts of linearized, inviscid stability theory, as shown by Rockwell[6], Sarohia[7], and Knisely and Rockwell[8]. As demonstrated by Knisely and Rockwell[8], on the basis of experiments interpreted with the aid of linearized theory, not only the fundamental component of the shear layer instability may be present, but a number of additional, primarily lower frequency components can exist as well. In fact, the magnitude of these components can be of the same order as the fundamental component. These issues have not been addressed for the case of a fully-turbulent in-flow and its separation from the leading corner of the cavity.

Related numerical simulations

In addition to the major elements contributing to onset of vortical structures in the separated shear-layer, as described in the foregoing, the possible modulation effect of the unsteady recirculating flow within the cavity should be addressed. Possible coupling between the unsteady flow structure within the cavity, in the form of recirculating eddies, and the unstable shear layer along the mouth of the cavity, has been the focus of a number of numerical investigations in recent years. Ghaddar, Korczak, Mikic and Patera[9] simulated the incompressible flow in periodically grooved channels by direct numerical simulation. A single, weak recirculating vortex is observed within the cavity. Najm and Ghoniem[10] employ a vortex simulation technique. They show that, for relatively short cavities, the roll-up of the instability of the separating shear layer is a dominant mode of oscillation, whereas for sufficiently long cavities, low frequency eddies within the cavity appear to dominate the oscillation mechanism. Pereira and Sousa[11] use a finite difference numerical scheme with temporal discretization. Patterns of instantaneous streamlines and vorticity contours within the cavity suggest a relationship to the unstable shear layer past the cavity. More recently, Pereira and Sousa[12] combine the results of their unsteady numerical simulation with pointwise laser-Doppler measurements at crucial locations in the cavity and suggest, for their particular cavity configuration and flow conditions, that coupling occurs between the shear layer and the dynamics of the recirculation flow field within the cavity. Most recently, Takaura,

Higashino, Yoshizawa, and Ogawa[13] have employed a large eddy simulation to determine the unsteady features of supersonic flow past a cavity. Their instantaneous patterns of velocity vectors within the cavity, at a time corresponding to inflow into the cavity at the impingement corner, exhibit a wall jet flow along the vertical and bottom faces of the cavity, which provides a mechanism for recirculation flow. The issue arises as to whether a fully-turbulent inflow at essentially zero Mach number gives rise to organized, large-scale recirculation zones within the cavity; if so, the manner in which they mimic the foregoing simulation is unclear.

Overview of available experimental information

Over the past few decades, considerable attention has been given to experimental characterization of self-sustained oscillations of impinging shear layers. These studies have been centered on pointwise measurements of pressure and/or velocity in qualitative flow visualization using dye, smoke or Schlieren techniques.

Visualization of the vortex interaction with the leading-edge of an impingement surface has been carried out by Ziada and Rockwell[14,15] and Tang and Rockwell[16] for the cases of a sharp impingement edge and the sharp corner of a cavity, respectively. Severe distortion of the incident vortices can occur and, in some cases, generation of secondary (counter) vortices plays a key role. Correspondingly, measurements of the fluctuating force on a wedge by Ziada and Rockwell[14] and pressure fluctuations on the surface of the corner by Tang and Rockwell[16] have shown the relationship between the phase of the induced force/pressure, the distortion of the incident vortex, and the generation of secondary vortices. Considerable insight has been provided by these visualization studies, which must be interpreted in accord with the issues and potential fallacies of qualitative flow visualization, as assessed by Gursul and Rockwell[17,18] and Gursul, Lusseyran, and Rockwell[19]. To complement qualitative visualization of the unsteady flow field immediately upstream and along the edge, Gursul and Rockwell[17] and Graf and Durgin[20] employ phase-averaged, phase-Doppler anemometry techniques to determine the cycle-averaged velocities adjacent to the edge for an elliptical leading-edge and a cavity-corner respectively.

Measurement of velocity fluctuations in the unsteady shear layer have been carried out using point-wise hot-wire, hot film and laser-Doppler anemometry techniques. Woolley and Karamecheti[21] determine the variation of the phase and amplitude of the velocity fluctuation along the shear layer of an impinging jet of a jet-edge system and Sarohia[7] characterized equivalent

quantities for the analogous oscillating shear layer of a shallow open cavity. Knisely and Rockwell[8] and Schachenmann and Rockwell[22] characterized the multiple frequency components and the streamwise distributions of organized wave amplitude and phase along open rectangular and closed axisymmetric cavities respectively. Gharib and Roshko[23] determined features of the velocity field in relation to the overall drag on the cavity. More recently, Pereira and Sousa[12], have obtained velocity spectra at selected locations in the cavity shear layer. These pointwise measurements, which have advanced our understanding of this class of flows, provide the stimulus for global, instantaneous measurements of the instantaneous flow structure.

Major unresolved physical and experimental issues

Essentially all quantitative measurements of the unsteady flow between the upstream (leading) corner in the downstream corner of the cavity have involved time-averaged or phase-averaged pointwise measurements. Even for the case of an initially laminar boundary layer at the upstream separation location, substantial "jitter", or cycle-to-cycle variation of the flow pattern, can occur for a typical cavity oscillation. Especially when the inflow boundary layer is transitional or turbulent, its coexistence with potentially coherent oscillations can generate very significant cycle-to-cycle variations of the flow pattern. It is therefore productive to obtain instantaneous measurements of the velocity field over the entire region of the flow. Such global realization would provide a physical basis for interpretation of various types of time-, ensemble-, and phase-averages of the flow structure. A further advantage is that instantaneous pressure fluctuations along the surface of the cavity can be directly related to instantaneous, global variations of the flow pattern. To date, this approach has not been undertaken, even for the simplest case of an initially-laminar flow at separation.

Impingement of a quasi-coherent, turbulent shear layer upon the downstream corner of the cavity will result in severe distortion of the incident vortical structures. These so-called turbulent vortices will have a range of scales. Instantaneous, global insight into the vortex distortion process is called for.

Amplification of disturbances in the separated turbulent shear layer along the cavity may involve coexisting instabilities, characteristic of a wide range of length scales present in the separating turbulent boundary layer and different characteristic thicknesses of the separating flow. The interaction of these instabilities in the evolving shear layer, i.e., small- and large-scale

interacting vortical structures, can most effectively be clarified using instantaneous, global representations of the flow structure, which has not yet been undertaken.

Within the cavity, existence of unsteady, recirculating flow is expected to occur in a highly modulated fashion, driven by the unsteady impingement process at the downstream (trailing) corner of the cavity. The instantaneous structure of these large-scale recirculating flows, and the manner in which they modulate the separating shear layer from the upstream (leading) corner of the cavity has not been addressed in a global, instantaneous sense.

Objectives

The overall goal of the present investigation is to address the unresolved issues defined in the foregoing. In general, this involves determining the instantaneous, global flow structure past and within a cavity due to an inflow turbulent boundary layer. The possible instantaneous, global states of the flow will be related to instantaneous pressure fluctuations on the downstream corner of the cavity. Furthermore, the time-averaged turbulence statistics will be interpreted in terms of these instantaneous flow patterns.

II. Experimental System and Techniques

Experiments were performed in a large-scale water channel, using combinations of surface pressure measurements and particle image velocimetry, which yielded global representations of the velocity and vorticity fields. The overall experimental system and quantitative measurement techniques are described in the following.

Experimental System

The free-surface water channel had a test section 36 inches wide × 24 inches deep. The total length of the test section was 20 feet. For the present experiments, the free-surface of the water was maintained at a height of 16.5 inches. This test section is preceded by a large contraction, having an inlet width of 6 feet; its contraction ratio is 2:1. An arrangement of honeycombs and screens is located upstream of the contraction; it minimized the free-stream turbulence, which is less than 0.1%. The freestream velocity was 10.53 inches/second.

The cavity test section, which was custom designed and constructed for the present experiments, was housed within the main test section of the water channel. Figure 2 shows the overall configuration and dimensions of the cavity section. It had an internal width of 18 inches

and an overall length of 130 inches. It is bounded on either side by vertical false walls extending from the floor of the water channel to a height equal to the upper edge of the channel test section. The cavity test section is preceded by a special inlet contraction, which has two purposes. First of all, it facilitates attainment of a higher velocity at the inlet of the cavity test section. Second, through use of a special gap arrangement between the inlet contraction and the leading-edges of the false walls of the cavity test section, it was possible to attain essentially parallel inflow into the leading region of the cavity test section (see plan view of Figure 2). This configuration is crucial, in that it precludes separation of the boundary layers along the interior surfaces of the false walls.

The major components of the cavity test section, most evident in the side view of Figure 2, involve a long flat plate, the cavity with an adjustable length L, and a deflection plate. A central objective of this unique facility is attainment of a turbulent boundary layer approaching the cavity. While experiments on flat plate boundary layers are abundant, the concept of employing such a plate with a rather complicated cavity arrangement had not been, up to the point of this experiment, attempted in any investigation. An important condition that must be satisfied is attainment of a stagnation point of the incident freestream at the tip of the elliptical leading-edge of the flat plate, having an aspect ratio of 4:1. This condition is essential if the boundary layer along the plate is to develop in a similar fashion as in a so-called infinite free-stream. Due to the difference in resistance between the regions above and below the flat plate, the stagnation point will, in the absence of any control device, be located along the lower surface of the elliptical edge, and induce a separation bubble along the upper surface of the leading-edge. This difficulty was overcome by employing a deflection plate at a location downstream of the cavity. It imposes an overall resistance on the upper region of the flow, such that the stagnation point is moved to the tip of the leading-edge of the plate generating the boundary layer.

In order to promote a fully-turbulent boundary-layer, the trip section was located immediately downstream of the leading-edge of the plate. Details of this trip section are described by Johansen and Smith[24]. Small (0.13 inch) and large (10.1 inch) diameter Plexiglas hemispheres were arranged in a spatially periodic pattern across the entire span of the plate. In the study of Johansen and Smith[24], this configuration was found to generate a well-posed turbulent boundary layer for the same value of flow velocity and effective plate length as employed in the present study.

Further details of the cavity system are described by Rockwell and Lin[25]. The laser sheet used for PIV was located at the midspan of the cavity test section. It was transmitted through the laser windows. These windows were 1/16 inch thick strips of Plexiglas, which were flush with the external surfaces of the cavity section. This thin Plexiglas minimizes laser refraction and transmission losses. The length L of the cavity was adjustable up to a maximum value of 16 inches. The effective depth W of the cavity was maintained constant of W = 4 inches for all experiments.

A transducer block built into the impingement corner housed a PCB high sensitivity transducer (Model No. 106B50), which measured the pressure fluctuations at the impingement corner of the cavity. It is described by Rockwell and Lin[25]. The pressure tap was located along the vertical face of the cavity corner at a distance of 0.13 inches below the corner and displaced a lateral distance of 0.57 inches. The transient response of this pressure tap-line-transducer system has a resonant frequency of 31 Hz, well above the frequencies of interest of this experiment, i.e., of the order of 1.0 Hz. The damping coefficient corresponded to maximum distortions of 0.5% of the pressure magnitude and phase.

Techniques of high-image-density particle image velocimetry

A custom-designed laser-optical arrangement was employed for generating the laser sheet employed for PIV measurements, based on the laser scanning concept described by Rockwell, Magness, Towfighi, Akin and Corcoran[26]. The entire optical system was mounted on a system of rails, allowing it to be translated to a specified location beneath the test section. A beam steering mirror and convex and concave lenses, having focal lengths f = 300 and 100 mm respectively, were fixed to this translating table. To facilitate further focusing and alignment of the rotating, multi-faceted mirror, it, along with a focusing singlet and a second beam steering mirror were all mounted on a circular table, which could be rotated to any angular position, relative to the large, translating table. In essence, this system allows the laser beam to be focused to a relatively narrow waist, with minimal distortion of the wave front less than $\lambda/10$ over the central region of the beam. With this particular lens combination, it was possible to attain the minimum waist of the laser beam at the half-vertical depth of the water channel test section. Simultaneously, the beam had a sufficiently small diameter as it impinged upon the face of a multi-faceted mirror, so that only one of the mirror facets was illuminated at a given instant of time.

The rotating mirror had seventy-two facets. Its speed of rotation was controlled by an external driver unit, such that the effective scanning frequency of the laser beam, 156.2 cycles/sec, generated optimum displacement between the multiply-exposed particle images during PIV experiments. The effective thickness of the scanned laser sheet formed by the scanning laser was 1.5 mm.

The laser beam emanated from a continuous wave Argon-ion having a variable output up to approximately 25 watts. For most of the experiments described herein, the effective output power of the laser was maintained at 15 watts. The water was seeded with metallic-coated particles having a diameter of 12 microns. Multiply-exposed images of these particles were recorded on high resolution film, having an effective resolution of 300 lines/mm. Two different types of 35 mm film cameras were employed during the course of this investigation. The first was a Nikon F-4 camera, which was employed for still photos of the inflow turbulent boundary layer and the cavity oscillation. The second camera was a Hulcher cinema camera, having a maximum framing rate of 60 frames per second. Extensive evaluation of the characteristic time scales of the cavity oscillation, in conjunction with the available lighting of the laser sheet, showed that a framing rate of 10 frames per second was optimal. Images were recorded on one hundred foot spools of 35 mm film. The pressure signal was recorded simultaneously during the cinema recording, in order to allow a direct correspondence between the pressure fluctuation at the corner of the cavity and the dynamics of the impinging shear layer. Full details of this cinema system are given by Lin and Rockwell[27].

For both camera systems, a rotating bias mirror, i.e. an image shifting mirror, was located in front of the camera lens, which had magnifications of 1:7.57 and 1:7.74. The mirror was oriented at an angle of 45°, and its angular displacement was triggered during each shutter opening, in order to impart a constant bias displacement of all particle images, which was removed during the interrogation process. The angular displacement of the mirror was of the order of 0.01°, in order to preclude systematic distortion effects of the pattern of particle images induced by finite rotation angle of the mirror.

Each 35 mm negative was digitized at a resolution of 125 pixels per millimeter. Then, these digitized image patterns were subjected to a single frame, cross-correlation technique, in order to provide the instantaneous velocity vector at each interrogation location. A 50% overlap of

interrogation areas was employed. The effective grid size in the plane of the laser sheet, i.e. the distance between velocity vectors, was 0.36 mm.

Post-processing of the raw velocity field involved, first of all, removal of bad vectors, then filling the blank location using a classical bilinear interpolation. The velocity field was smoothed using a Gaussian filter having an exponent p = 1.3. These interpolation and filtering techniques are well known and described in detail by Landreth and Adrian[28].

Pressure and Velocity Measurements

Time traces of the pressure fluctuations were acquired with a PCB pressure transducer having a sensitivity of 500 mv/psi. During experiments, the pressure signal was subjected to analog filters and electronic amplifiers. The sampling time was $\Delta t = 0.004$ sec, in order to adequately resolve all the dominant frequencies. The signal was transmitted to the A/D board of the host microcomputer, stored in digital form, allowing reconstruction of the time traces, as well as computation of the power spectral density using an FFT technique. The total acquisition time T of each velocity and pressure record depended upon the particular experiment. Its value, along with the effective sampling time Δt and sampling frequency Δf are specified in conjunction with each of the time traces and spectra presented in the following.

III. Inflow Turbulent Boundary Layer

The turbulent boundary layer approaching the cavity was characterized upstream of the separation corner of the cavity. Using the coordinates (x,y) centered at the separation point of the leading corner of the cavity, PIV images were acquired over the spatial domain extending from $x = -10.31$ inches to $x = -14.87$ inches and from $y = 0.018$ to 3.02 inches. A typical instantaneous velocity field, in a reference frame of observation of $0.8\ U_\infty$, where U_∞ is the freestream velocity, is shown at the top of Figure 3.

A total of thirty-eight PIV images were acquired at random times, with a minimum spacing of 60 sec. The variation of the velocity with coordinate x was considered at a given y in a specified image, and the values of the mean velocity components $\overline{u}$, $\overline{v}$, the corresponding fluctuation components u_{rms} and v_{rms}, as well as the velocity correlation $\overline{u'v'}$, were determined for that image. Then, by averaging these values in all thirty-eight images, the final statistical values were

obtained. This approach is described by Liu, Landreth, Adrian and Hanratty[29] and Westerweel, Draad, van der Hoevern and van Oord[30].

Figure 3 shows the variation of the mean, fluctuation and correlation quantities across the boundary layer. For these data, the boundary layer thickness δ = 1.80 inches, the displacement thickness δ^* = 0.27 inches, momentum thickness θ = 0.197 inches, and the shape factor $H = \delta^*/\theta = 1.37$. The Reynolds number based on momentum thickness was $Re_\theta = 1{,}371$. At this value of Re_θ, Johansen and Smith[28] obtained H = 1.37 via single point hot film measurement.

Comparison of these distributions with those of Klebanoff[31] (see also Schlichting[32], acquired using a hot wire anemometer, indicates remarkably good agreement. Further details and comparisons of the turbulent boundary-layer structure are given by Rockwell and Lin[25]. To demonstrate that a well-defined log layer exists within the turbulent boundary layer, the raw data of the present study, in the form $\overline{u}/U_\infty$ versus y (in mm) was plotted on semi-log coordinates. A well-defined log region was shown to exist.

Moreover, to ascertain that a well-defined inertial subrange existed within the turbulent boundary layer, the PIV data were further evaluated. For each of the thirty-eight images, the spectrum was evaluated at a distance 0.91 inches from the wall corresponding to 0.5 δ, in which δ is the boundary layer thickness, also represented by the symbol δ_{995}. The technique for evaluation of the spectra is described in Section II. In essence, at each elevation from the wall, the entire sequence of u or v velocity components was considered from the left to the right boundary of the image. This sequence is, in essence, interpreted as a time sequence, leading to a frequency spectrum. Spectra for both the streamwise u′ and cross-stream v′ fluctuations were calculated. Figure 4 shows the well-known slope in the inertial subrange, n = −5/3, on the spectrum. It extends over the range $20 \leq 2\pi f\, \delta_{995}/U_\infty \leq 10^2$. This range of agreement is remarkably coincident with, for example, the normalized plot of Bradshaw[33]. At lower values of dimensionless frequency, however, there is a degree of scatter within the data, due to the fact that the averaging process did not include a sufficiently large number of images. Furthermore, at relatively high values of dimensionless frequency, the spectra of Figure 4 are meaningless, due to the fact that the spatial resolution Δx of the PIV image cannot properly represent the smallest scales of the turbulence.

IV. Instantaneous Flow Structure and Pressure Fluctuations

Sequences of instantaneous PIV images were obtained using two approaches. The first involved a cinema PIV sequence. In this case, images were acquired at a framing rate of ten frames per second, yielding a total of 167 images with a time increment $\Delta t = 0.1$ seconds between them. The second approach involved random acquisition of 77 images, whereby the camera was triggered at an arbitrary time, with the only constraint that the interval between successive images exceeded 60 seconds, which is approximately a factor of 12 longer than the period of the lowest, coherent spectral component at 0.2 Hz.

In order to establish the relationship between the fluctuation pressure at the trailing-corner and the distortion of the flow structure in that region, the pressure at tap B was acquired simultaneously with the cinema PIV series. The time trace is shown in Figure 5. The framing rate of the cinema sequence is 10 frames/sec and the first image of the cinema sequence corresponds to the instant $t = 0.1$ sec in the time trace of pressure. Subsequent images in the cinema sequence correspond to $t = 0.2$, $t = 0.3$ sec and so on in the pressure trace. A complete collection of the cinema images is given in Rockwell and Lin[25]. In the following, selected images and corresponding pressure traces are shown to illustrate the major features of the cavity oscillation.

The time trace of the pressure fluctuations shown in Figure 5 exhibits substantial modulation of the period between successive peaks. It is possible to identify portions of the trace that have a peak to peak spacing corresponding to the fundamental β and subharmonic $\beta/2$ of the most unstable frequency of the shear layer. These modes are designated as $1/\beta$ and $2/\beta$. The circle symbols indicated at the minimum or maximum values of the pressure trace correspond to the cinema images that are examined in detail in the following.

Comparison of the pressure at the impingement corner with the instantaneous vorticity and velocity distributions is given in Figure 6a. The position of the pressure tap is 0.13 inches below the tip of the corner. At the instant shown in Figure 6a, the pressure has a maximum-negative value. Correspondingly, the cluster of vorticity has its center approximately coincident with the location of the pressure tap. The impinging vortex is actually made up of layers of small-scale vortical structures. The overall diameter of this vortex is of the order of one-half the cavity length. The corresponding velocity field suggests an upward-oriented outflow from the cavity at the trailing-corner. This apparent outflow is, of course, associated with the arrival of the cluster

of vorticity at the corner. Within the cavity, jet-like flow along the vertical and bottom wall is clearly evident. Moreover, the upward oriented velocity field over the first half of the cavity length is in accord with the large entrainment demands over the initial extent of the separated shear layer formed from the leading-corner of the cavity.

Of course, it is well-known that the interpretation of patterns of velocity vectors and streamlines is dependent upon the reference frame of observation. For this reason, the velocity field of the separated layer and its impingement upon the corner of the cavity is visualized in not only the laboratory frame, but also frames moving at 0.25 and 0.50 U_∞ as shown in Figure 6b. At a frame velocity of 0.25 U_∞, the swirl patterns of velocity vectors correspond well to the concentrations of vorticity shown in Figure 6a. In Figure 6b, the extent of the distorted vortex upstream of, and above, the trailing-corner of the cavity, in accord with the cluster of vorticity in Figure 6a, is particularly evident.

In Figure 7, the incident cluster of vorticity is located just upstream of the corner. The small-scale concentrations that make up the large-scale structure are identified, in an approximate sense, by the dashed circle. In this case, the instantaneous pressure takes on its maximum-positive value, and the velocity field in the vicinity of the corner shows a downward deflection and formation of a pronounced, jet-like flow along the vertical wall of the cavity.

Instantaneous patterns of velocity and vorticity for the cavity oscillation in a mode corresponding to approximately the subharmonic frequency $\beta/2$ are shown in Figures 8 and 9 for the maximum-negative and -positive values of pressure at the impingement corner. Figure 8 shows images corresponding to the maximum-negative pressure peak, where the center of the vorticity cluster is nearly coincident with the location of the pressure tap at the corner. In this case, the velocity field exhibits a particularly violent ejection of fluid out of the cavity, drawn upward by rotation of the large-scale cluster of vorticity as it encounters the corner. In Figure 9, corresponding to the maximum-positive pressure peak, the cluster of incident vorticity is located upstream of the cavity face. The interesting feature of this particular vortex-corner interaction is that the entire extent of the flow, from the bottom of the cavity to the separated shear layer, is part of a large-scale swirl pattern, suggesting coupling between the large-scale cluster of vorticity approaching the corner and the recirculation flow in the right half of the cavity.

Viewing the relationship between the large-scale clusters of vorticity in the vicinity of the corner and the induced pressure at the corner, shown in Figures 6 through 9, the common feature is that when the center of the large-scale vorticity cluster is approximately coincident with the cavity corner, a maximum-negative pressure is induced at the corner, whereas when it is at a location just upstream of the corner, the pressure takes on its maximum-positive value. These observations are in accord with those of Tang and Rockwell[16] for the case of an unstable laminar shear layer, which generated identifiable vortical structures that impinged upon the corner of the cavity. From the present study, it appears that this process of vortex-corner interaction is associated with substantial variations in outflow and inflow into the cavity as the vortex approaches and is severely distorted in the corner. Further consideration of this detailed interaction should provide insight into the character of the pressure source(s) that is crucial in determining the upstream influence and, especially at higher Mach number, the nature of the radiated sound pattern.

Regarding the flow field within the cavity, Figure 10 compares the instantaneous velocity of Figure 9 with the calculation of Takakura, Higashino, Yoshizawa, and Ogawa[13], for which the flow exterior to the cavity was supersonic. Nevertheless, the overall features of the velocity pattern within the cavity are remarkably similar: (i) the large magnitudes of the velocity vectors, oriented downward and away from the vertical face of the cavity; (ii) the jet-like flow along the bottom wall of the cavity, having a nearly discontinuous leading-front, i.e., the magnitude of the front edge of this jet-like flow abruptly decreases in magnitude; (iii) an upward jet-like flow along the vertical face of the leading-corner of the cavity; and, finally, (iv) a pronounced recirculating, vortex-like, flow over the right-half of the cavity, extending from the bottom wall to the separated shear layer.

Comparison of a representative image from the cinema sequence with an excerpt from the unsteady numerical simulation of Pereira and Sousa[12] is given in Figure 11. In making this comparison, an image from the cinema sequence was selected to match the phase of the oscillatory shear-layer of the numerical simulation. Both images of Figure 11 exhibit: (i) small-scale vorticity concentrations immediately downstream of separation from the leading-corner of the cavity; (ii) appearance of an initial cluster of vorticity; (iii) a thin, elongated region of vorticity between this impinging vortex and the small-scale clusters of vorticity located upstream of it; and

(iv) an approximately vertical orientation of a large-scale cluster of vorticity as it encounters the trailing-corner of the cavity. It should be noted, however, that the patterns of recirculating vortices within the cavity are significantly different.

V. Averaged Flow Structure

Representations of the averaged flow pattern were obtained by averaging a series of instantaneous images of the type shown in Section 4. The first averaging involved consideration of the entire set of images in the cinema sequence. A total of 167 images was acquired at a time interval $\Delta t = 0.1$ sec between images. Accounting for the fact that 167 images were acquired, then the total time of acquisition corresponds to 16.7 sec. Recall from the cinema pressure trace, as well as other related traces, that the cavity oscillation appears to exhibit a competition between the fundamental at approximately 1.0 Hz and the subharmonic at about 0.5 Hz. This means that the cinema signal corresponds to 16.7 cycles of the fundamental and 8.35 cycles of the subharmonic.

The second type of average involved randomly selected images, as opposed to foregoing sequence of images, which were closely-spaced in time. A total of 77 images were acquired for this averaging. In this case, the minimum Δt between images was 60 sec., which was approximately a factor of 12 longer than the period corresponding to the lowest organized component in the spectrum, i.e., the component at approximately 0.2 Hz. This random sampling is typical of that employed in turbulent flows. An example is the averaged turbulent statistics of a turbulent jet impinging upon a plate involving 11 images (Landreth and Adrian[34]).

Calculation of the averaged quantities was performed according to the equations listed below. Each averaged parameter was calculated at each spatial coordinate (x,y) by considering the average of all instantaneous values (x,y). The terminology for each of the averaged parameters and the dimensionless equation employed to determine the averaged parameter are as follows:

$< V >$ ≡ averaged (or mean) total velocity

$$< V > \equiv \frac{1}{N}\sum_{n=1}^{N} V_n(x,y) \tag{5.1}$$

$< u >$ = averaged value of streamwise component of velocity

$$< u > \equiv \frac{1}{N}\sum_{n=1}^{N} u_n(x,y) \tag{5.2}$$

$< v >$ = averaged value of transverse component of velocity

$$< v > \equiv \frac{1}{N}\sum_{n=1}^{N} v_n(x,y) \tag{5.3}$$

$< \omega >$ = mean value of vorticity ω

$$< \omega > \equiv \frac{1}{N}\sum_{n=1}^{N} \omega_n(x,y) \tag{5.4}$$

$< u'v' >$ = averaged value of Reynolds stress correlation

$$< u'v' > \equiv \frac{1}{N}\sum_{n=1}^{N} [u_n(x,y) - < u(x,y) >][v_n(x,y) - < v(x,y) >] \tag{5.5}$$

The averaging process involved, in essence, stacking a series of instantaneous images in evaluating the averaged parameter at a given location (x,y). This type of average is referred to as an ensemble-average. We emphasize that, unlike some ensemble-averaging processes, no phase reference or phase trigger was employed. Rather, in the case of the randomly-acquired images, the camera was triggered at an arbitrary time, so long as the interval between images was greater than 60 sec. For the cinema series, no phase condition was employed. It is important to realize, however, that, for the cinema series, the time spacing between successive images employed in the ensemble-averaging process is 0.1 sec, which corresponds to approximately 1/10th of the fundamental instability frequency β and 1/2 of the lowest coherent spectral component at 0.2 Hz.

Since markedly different criteria were employed for the acquisition of images corresponding to the two types of averages described in the foregoing, a direct comparison of the averaged quantities should provide an indication of the degree of convergence. For this reason, averaged images obtained from the cinema series are directly compared with those from the randomly-acquired series in Figures 12 through Figure 14. Each figure contains two averaged images. The top one corresponds to that obtained from the cinema sequence, while the lower one represents the randomly-sampled (acquired) sequence.

When examining and comparing the images of Figures 12 through 14, issues related to the process of image acquisition should be kept in mind. Narrow shadow regions exist immediately above the leading- and trailing-corners of the cavity. Whereas the bilinear interpolation process was effective in providing accurate distributions of velocity through the

shadow region above the trailing-corner, no attempts were made to refine the distortion due to the shadow region above the leading-corner of the cavity. The width of this shadow region is 0.008 L, where L is the cavity length. This region is not essential to understanding the central physical features of interest herein; moreover, the characteristics of the inflow boundary layer are already known from independent boundary layer measurements taken well upstream of the cavity. It is also evident, in a number of the averaged images, that the outline of the cavity is slightly tilted relative to the horizontal. This is simply due to the fact that, especially for the cinema camera, it was very difficult to perfectly align the bottom wall of the cavity with the lower boundary of the field of view. This slight tilting does not, however, affect the quality or accuracy of the PIV data.

Averaged (mean) velocity

Comparison of the averaged total velocity $< V >$ for the cinema and randomly-acquired image sequences, corresponding to the top and bottom images respectively, is given in Figure 12. It is evident that these patterns of $< V >$ are remarkably similar. It should be noted that the apparent difference in the first line of velocity vectors in the turbulent boundary layer, emanating from the leading-corner of the cavity, is simply due to a different starting point for construction of these velocity vectors. Particularly interesting is the flow in the immediate vicinity of the corner of the cavity. It makes an abrupt transition from vectors that are predominantly oriented in the vertical direction, to those that are essentially in the horizontal direction, over a very small distance. This occurs at a streamwise location immediately downstream of the leading-corner of the cavity, and corresponding to large values of mean vorticity. This severe distortion of the mean flow, which occurs over a relatively small characteristic thickness is most likely linked to the rapid onset of the small-scale vortical structures, which appear immediately downstream of the leading-corner of the cavity, evident, for example, in Figures 6a and 8. In the vicinity of the trailing-corner of the cavity, the continuous line of velocity vectors that impinges directly upon the vertical face of the cavity, at a location immediately below the trailing-corner, represents the averaged stagnation streamline. Below this line, flow is into the cavity. This downward-deflected flow forms a jet that continues along the bottom surface of the cavity. Eventually this fluid is drawn upward towards the separating shear layer along the mouth of the cavity, in order to satisfy

entrainment demands. Overall, the flow pattern in the right half of the cavity appears to exhibit a large-scale recirculation flow, which might loosely be termed a recirculation vortex.

This averaged pattern of total velocity $< V >$ in the cavity, more specifically, the large-scale recirculating vortex, is in accord with certain features of recent numerical simulations. The occurrence of a single, large-scale vortex is discernible in the averaged streamline patterns (with superposed pressure intensity contours) of Takakura, Higashino, Yoshizawa, and Ogawa[13]. Moreover, the time sequence of instantaneous streamline patterns of Pereira and Sousa (1993) suggests, when averaged, that a single, large-scale vortex would dominate. The instantaneous streamline plots of the subsequent study of Pereira and Sousa[12] (not shown) exhibit a second, weaker vortex.

Averaged vorticity

Contours of constant averaged vorticity $< \omega >$ are indicated in Figure 13. Concerning the region of the separated layer extending from the leading- to the trailing-corner of the cavity, it is evident that the vorticity levels dominate those of the background turbulent boundary layer. Very high levels of vorticity are generated immediately downstream of the corner, where the flow makes an abrupt transformation from an attached to a separated layer. Regarding the region within the cavity, positive vorticity of significant magnitude extends well upstream along the bottom wall of the cavity.

Velocity correlation

Distributions of the velocity correlation $< u'v' >$ are given in Figure 14. In the separated shear layer between the leading- and trailing-corners of the cavity, small-scale regions of relatively high correlations of $< u'v' >$ suggest the existence of a number of small-scale vortical structures along the shear layer, already evident in, for example, the vorticity distributions in Section 4. The peak values of $< u'v' > / U_\infty^2$ in this separated layer are of the order of 10^{-2}. This value compares with the peak value in a free, turbulent mixing-layer of about 2×10^{-2} (Fiedler, Dziomba, Mensing, and Rösgen[35]). They exceed the maximum values in the approach turbulent boundary layer by a factor of approximately 7 (compare Figure 3). This observation again suggests dominance of the dynamics of the separated shear layer over the background turbulent boundary layer. Within the cavity, along the vertical face, large amplitudes of the $< u'v' >$ correlation of

opposite sign occur over nearly its entire extent. By comparison with the mean velocity $<V>$ plots of Figure 12, it can be seen that the extrema of these $<u'v'>$ contours occur along the edge of the jet-like flow along the vertical face. Hussain[36] has shown, for a free axisymmetric, that either positive or negative regions of Reynolds stress may occur due to vortex interactions; counter-gradient average momentum transport is therefore possible. Similarly, high levels of $<u'v'>$ occur along the bottom wall of the cavity; again, the location of these extrema approximately correspond to the edge of the jet-like flow. The loci of these extrema along the edge of the wall jet within the cavity are directly analogous to that along the bottom edge of the separated layer extending from the leading- to the trailing-corner of the cavity, and are in accord with the well-known observation of high levels of Reynolds stress occurring along the edge of a separated layer, due to generation of vortical structures in that region (Fiedler, Dziomba, Mensing, and Rösgen[35]).

VI. Assessment of Major Results

This investigation, which has provided instantaneous images of the flow structure, allows insight well beyond that attainable using traditional experimental techniques involving, for example, dye visualization, smoke injection and hydrogen bubble visualization. The quantitative velocity and vorticity fields and their evolution with time provide the basis for image evaluation with an eye towards identifying key pressure sources. The major features of the unsteady separated shear-layer along the cavity, its interaction with the corner of the cavity, and the corresponding flow within the cavity have been revealed, and their primary features will dictate the nature of the unsteady pressure field immediately adjacent to and well away from the cavity configuration.

In the following, summaries and assessments of the principal regions of the flow are provided.

Structure of separated shear-layer along cavity

Instantaneous images of the vorticity field reveal that the separated shear-layer exhibits two categories of coherent vortical structures. The first involves small-scale concentrations of vorticity, which are rapidly formed from the leading-corner of the cavity, and have a wavelength substantially smaller than the cavity length. The second takes the form of a large-scale cluster of

vorticity, which actually results from agglomeration of the small-scale concentrations. The typical wavelength between these large-scale structures is of the order of the cavity length, and their development appears to be analogous to the roll-up of vortices in a laminar shear layer past a cavity at substantially lower values of Reynolds number.

These observations suggest the existence of two instabilities in the cavity shear layer. The initial, small-scale instability is expected to scale with a local thickness immediately in the vicinity of the leading-corner of the cavity. An approach to predicting the most unstable frequency of the inner region of the shear layer involves use of the vorticity thickness $\delta_\omega = (U_1 - U2)/(dU/dy)_{max}$, in which U_1 and U_2 are the velocities on the upper and lower sides of the inner portion of the free layer at a location immediately downstream of separation and $(dU/dy)_{max}$ is the maximum value of vorticity within the layer. Using this characteristic thickness, one could determine the most unstable frequency of the small-scale vortical structures immediately downstream of separation from the leading-corner of the cavity. This approach directly shows the consequence of the very high level of mean vorticity at the leading corner of the cavity. Now consider the instability leading to formation of the large-scale clusters of vorticity, which is of the convective type, and is reinforced through feedback from the vortex-corner impingement to the upstream (leading-) corner of the cavity. The formation of these large-scale vorticity clusters occurs at the dimensionless frequency β. If we employ the momentum thickness θ_0 of the turbulent boundary layer at separation, and view it as an approximation to the value of θ at a representative downstream location, where this larger scale instability develops, it is possible to account for the entire transverse extent of the shear layer in predicting the frequency β. According to linear stability theory for a convective-type instability, the dimensionless frequency should be $\beta = f\theta/U_\infty = 0.017$. Using the value of θ at separation, i.e. θ_0, and the free-stream velocity U_∞ defined in Section 2, the predicted frequency is $f = 0.908$ Hz, which is very close to the typical peaks having a spacing corresponding to approximately 1.0 Hz in the time traces of Figure 5. Moreover, the subharmonic component $\beta/2$ has a frequency roughly half the value in the time traces. It is important to note that the classical process of successive vortex coalescence leading to larger scale vortical structures in a free shear layer originates with an instability at dimensionless frequency $\beta \cong 0.017$ when the boundary layer is laminar. The estimated frequency of the aforementioned small-scale vortices gives a value of β nearly an order of magnitude larger when the momentum thickness θ_0 is employed at separation.

On the other hand, immediately downstream of the leading-corner, the value of peak mean vorticity drops substantially (again, compare Figure 13). If we approximate the so-called free-stream velocity on the lower side of the separated layer U_2 as equal to zero and that along the upper side U_1 as remaining relatively constant with streamwise distance at a value U_∞, it follows that the vorticity thickness δ_ω in the immediate vicinity of the corner will be substantially lower than that in the region downstream of the corner. In turn, the predicted instability frequency for the small-scale vortex formation from the corner will be substantially higher than that in the region downstream of the corner, which is more characteristic of the global-type instability of the entire separated layer.

An additional mechanism that may produce the patterns of small-scale vortical structures at the leading-corner of the cavity is the existence of hairpin vortices in the fully turbulent boundary layer upstream of the leading-corner of the cavity. Multiple hairpin structures having a streamwise spacing of the order of one-tenth the boundary layer thickness are evident in the PIV images of Figures 7 through 9. This possibility should be investigated further in conjunction with the aforementioned mechanism of a small-scale instability.

The foregoing mechanisms of vortex formation in the separated shear layer coexist with and, in some cases may be coupled with, the large-scale patterns of recirculating flow within the cavity. Recent numerical simulations of Pereira and Sousa[12] and Najm and Ghoniem[10] specifically address the potential role of the large-scale vortex within the cavity. In fact, by viewing this region of the flow as a nonlinear dynamical system, it is possible to define a mechanism of instability due to the recirculating vortex system. The degree of predominance of this type of instability is not completely resolved. It is evident, however, by inspection of a time sequence of instantaneous images, that the velocity and pressure signals exhibit substantial modulation, or even intermittency, which may be due, at least in part, to the character of the recirculating flow within the cavity. We note, that in the low Reynolds number study of Knisely and Rockwell[8], involving flow past a cavity, that the spectra of the velocity and pressure fluctuations can exhibit a substantial number of peaks due to modulation phenomena. From the standpoint of shear layer stability, an important finding from their study is that several of the spectral components can simultaneously satisfy the phase-locking criterion between the leading- and trailing-corners of the cavity, emphasizing the importance of the instability mechanism of the separated shear layer.

The importance of the onset and development of clusters of vorticity, associated with the inherent instability of the shear-layer, is further evident from examination of the contours of constant dimensionless Reynolds stress of Figure 14. The peak values overshadow those of the inflow turbulent boundary layer, due to the coherent development of vortical structures in the separated layer.

Structure of shear-layer interaction with corner of cavity

The instantaneous velocity and vorticity fields presented herein provide the first quantitative definition of the distortion of the shear layer, more specifically of the large-scale clusters of vorticity as they encounter the corner of the cavity. As these clusters of vorticity interact with the corner, it is possible to identify large variations in inflow and outflow, to and from, the interior of the cavity. This information should be helpful in formulating models for the source of pressure fluctuations at the corner that are crucial in determining the far field sound radiation. The importance of considering different reference frames of observation of the instantaneous velocity field has been emphasized. Depending upon the frame, different features of the cavity shear layer are emphasized. Further assessment of the data in the vicinity of the cavity corner should involve: (i) calculation of pressure source terms; and (ii) construction of instantaneous streamline patterns in various reference frames, then with the aid of critical point theory, interpreting the time-variation of critical points in conjunction with magnitudes of pressure source terms in that region.

By simultaneously recording the pressure trace at the impingement corner with the cinema PIV sequence, it has been possible to determine the phase relationship between the arrival and distortion of the large-scale clusters of vorticity and the maxima and minima of the pressure fluctuations at the corner. The issue arises as to what types of geometrical modifications of the corner could serve as a basis for attenuation of the surface pressure fluctuations in that region.

The classical, time-averaged viewpoint of a cavity flow is that suggested in the averaged images of Figure 12. By constructing tangents to the velocity vectors, it is possible to identify a stagnation or reattachment streamline at the corner. Any given instantaneous image, however, does not show existence of such a reattachment line, rather the distortion of the incident vortical structures in that region, in conjunction with instantaneous inflow or outflow provide a very different picture than the averaged representation. This sort of interpretation is important for a wider class of separated and reattaching flows, such as that behind a backward facing step.

Structure of flow within cavity

The flow pattern within the cavity is dominated by a jet-like flow along the vertical wall of the trailing-corner, then in the upstream direction along the bottom wall of the cavity. This jet-like flow is a sort of wall jet, having a boundary layer on one side and a free, separated layer on its other side. This free shear-layer exhibits detectable vortical structures, which serve as a source of substantial velocity fluctuations and represent the loci of maximum velocity correlations $< u'v' >$. In general, the flow rate associated with this jet-like flow into the cavity must satisfy the entrainment demands of the separated shear layer between the leading- and trailing-corners of the cavity. In many of the instantaneous images, this upward-oriented entrainment flow is evident along a substantial length of the separated layer. In addition, however, an upward-oriented, jet-like flow along the vertical face of the leading-corner of the cavity influences the initial development of the separating turbulent boundary layer. Unsteadiness of this upward-oriented jet no doubt contributes to the modulated character of the separated layer.

A number of admissible patterns of instantaneous, recirculation vortices can occur within the cavity. These recirculation vortices tend to occupy the right half of the cavity. In the limiting case, the swirl pattern of velocity vectors associated with this recirculation vortex extends from the bottom wall of the cavity to the separated layer, suggesting a coupling between the recirculation vortex and the large-scale cluster of vorticity that impinges upon the cavity corner. Further analysis of the data should provide insight into the possibility of such coupling.

VII. Conclusions

The central findings of the present investigation are as follows:

(1) A fully turbulent inflow, in the form of a turbulent boundary layer separating from the leading-corner of the cavity, can evolve into a pattern of organized vortical structures. Two extreme scales of these structures have been identified. The largest-scale structures scale according to the momentum thickness of the time-averaged velocity distribution at the leading-corner of the cavity. The corresponding dimensionless frequency of formation of these large vortical structures is in close agreement with that predicted from inviscid stability theory. In addition, organized vortical structures of a much smaller scale form from the leading-corner of the cavity. In this region the mean vorticity is very high and the

corresponding local vorticity thickness of the separated layer will be relatively small, thereby promoting formation of small-scale vortical structures at relatively high frequency. The possible role of pre-existing vortical structures in the approach turbulent boundary layer, and their relation to those observed from the leading-corner of the cavity remains for further investigation.

(2) The separated shear layer exhibits a complex modulated structure, evident in not only the instantaneous PIV images, but also in the time traces of the pressure signal at impingement. The latter exhibits both amplitude- and frequency-modulated features, but, generally speaking, such traces exhibit periods corresponding to the fundamental and subharmonic of the instability mode associated with formation of the largest-scale vortical structures. The physical origin of this modulation is, at least in part, due to a modulated, jet-like return flow within the recirculation zone of the cavity. A front of such a jet is produced when a portion of the unsteady shear layer is deflected downward into the cavity at the location of the impingement corner.

(3) The time-averaged characteristics of the shear layer along the cavity, as well as recirculating flow within the cavity, are expressed in terms of Reynolds stresses, time-Reynolds stresses, vorticity and velocity. It is demonstrated that the Reynolds stresses of the shear layer along the cavity rapidly dominates those of the approach turbulent boundary layer. The patterns of averaged vorticity show that the region of separation from the leading-corner of the cavity dominates all other regions of the flow field, including the shear layer along the cavity and the recirculating flow within the cavity.

VIII. Acknowledgements

The authors gratefully acknowledge the partial support, in the form of research instrumentation and equipment, from National Science Foundation Grants, CTS-9422432 and CTS-9803734, Office of Naval Research Grant N00014-1-0815, and the Air Force Office of Scientific Research, Grant No. F49620-00-1-0009.

IX. List of References

[1]Rockwell, D. and Naudascher, E., "Review - Self-Sustaining Oscillations of Flow Past Cavities", *Transactions of the ASME, Journal of Fluids Engineering*, Vol. 100, June, 1978, pp. 152-165.

[2]Rockwell, D. and Naudascher, E., "Self-Sustained Oscillations of Impinging Free Shear Layers", *Annual Review of Fluid Mechanics*, Vol. 11, 1979, pp. 67-94.

[3]Rockwell, D., "Invited Lecture: Oscillations of Impinging Shear Layers", *AIAA Journal*, Vol. 21, No. 5, 1983, pp. 645-664.

[4]Howe, M. S., "Edge, Cavity, and Aperture Tones at Very Low Mach Numbers", *Journal of Fluid Mechanics*, Vol. 33, 1997, pp. 61-84.

[5]Rockwell, D., "Vortex-Body Interactions", *Annual Review of Fluid Mechanics*, Vol. 30, 1998, pp. 199-229.

[6]Rockwell, D., "Prediction of Oscillation Frequencies Due to Unstable Flow Past Cavities", Transactions of the ASME, *Journal of Fluids Engineering*, Vol. 99, June, 1977, pp. 294-300.

[7]Sarohia, V., "Experimental Investigation of Oscillations in Flows Over Shallow Cavities", *AIAA Journal*, Vol. 15, No. 7, July, 1977, pp. 984-991.

[8]Knisely, C. and Rockwell, D., "Self-Sustained Low-Frequency Components in an Impinging Shear Layer", *Journal of Fluid Mechanics*, Vol. 116, 1982, pp. 157-186.

[9]Ghaddar, N. K., Korczak, K. Z., Mikic, B. B. and Patera, A. T., "Numerical Investigation of Incompressible Flow in Grooved Channels. Part 1. Stability and Self-Sustained Oscillations", *Journal of Fluid Mechanics*, Vol. 163, 1986, pp. 99-127.

[10]Najm, H. N. and Ghoniem, A. F., "Numerical Simulation of the Convective Instability in a Dump Combustor", *AIAA Journal*, Vol. 29, No. 6, June, 1991, pp. 911-919.

[11]Pereira, J. C. F. and Sousa, J. M. M., "Finite Volume Calculations of Self-Sustained Oscillations in a Grooved Channel", *Journal of Computational Physics*, Vol. 106, 1993, pp. 19-29.

[12]Pereira, J. C. F. and Sousa, J. M. M., "Experimental and Numerical Investigation of Flow Oscillations in a Rectangular Cavity", *Transactions of the ASME, Journal of Fluids Engineering*, Vol. 117, March, 1995, pp. 68-74.

[13]Takakura, Y., Higashino, F., Yoshizawa, T. and Ogawa, S., "Numerical Study on Unsteady Supersonic Cavity Flows", AIAA Paper 96-2092, 27th AIAA Fluid Dynamics Conference, June 17-20, 1996, New Orleans, LA.

[14]Ziada, S. and Rockwell, D., "Vortex-Leading Edge Interaction", *Journal of Fluid Mechanics*, Vol. 118, 1982a, pp. 79-107.

[15]Ziada, S. and Rockwell, D., "Oscillations of an Unstable Mixing Layer Impinging Upon a Wedge", *Journal of Fluid Mechanics*, Vol. 124, 1982b, pp. 307-334.

[16]Tang, Y.-P. and Rockwell, D., "Instantaneous Pressure Fields at a Corner Associated with Vortex Impingement", *Journal of Fluid Mechanics*, Vol. 126, 1983, pp. 187-204.

[17]Gursul, I. And Rockwell, D., "Vortex Street Impinging Upon and Elliptical Leading-Edge", *Journal of Fluid Mechanics*, Vol. 211, 1990, pp. 211-242.

[18]Gursul, I. and Rockwell, D., "Effect of Concentration of Vortices on Streakline Patterns", *Experiments in Fluids*, Vol. 10, 1991, pp. 294-296.

[19]Gursul, I., Lusseyran, D., and Rockwell, D., "On Interpretation of Flow Visualization of Unsteady Shear Flows", *Experiments in Fluids*, Vol. 9, 1990, pp. 257-266.

[20]Graf, H. R. and Durgin, W. W., "Measurement of a Non-Steady Flow Field in the Opening of a Resonating Cavity Excited by Grazing Flow", *Journal of Fluids and Structures*, Vol. 7, 1993, pp. 387-400.

[21]Woolley, J. P. and Karamcheti, K., "Role of Jet Stability in Edge-Tone Generation", *AIAA Journal*, Vol. 12, November, 1974, pp. 1457-1458.

[22]Schachenmann, A. and Rockwell, D., "Self-Generation of Organized Waves in an Impinging Turbulent Jet at Low Mach Numbers", *Journal of Fluid Mechanics*, Vol. 117, 1982, pp. 425-441.

[23]Gharib, M. and Roshko, A., "The Effect of Flow Oscillations on Cavity Drag", *Journal of Fluid Mechanics*, Vol. 177, 1987, pp. 501-530.

[24]Johansen, J. B. and Smith, C. R., "The Effects of Cylindrical Surface Modifications on Turbulent Boundary Layers", Report FM-3, Department of Mechanical Engineering and Mechanics, Lehigh University, Bethlehem, PA., April, 1983.

[25]Rockwell, D. and Lin, J.-C., "Experimental data for computational fluid dynamic simulations of fluid oscillators: cavity flow. Volumes 1 and 2", Fluid Mechanics Laboratories Report R01, 1996, Department of Mechanical Engineering and Mechanics, Lehigh University, Bethlehem, Pennsylvania, U.S.A., 1996.

[26]Rockwell, D., Magness, C., Towfighi, J., Akin, O. and Corcoran, T., "High Image-Density Particle Image Velocimetry Using Laser Scanning Techniques", *Experiments in Fluids*, Vol. 14, 1993, pp. 181-192.

[27]Lin, J.-C. and Rockwell, D., "Cinema PIV and Its Application to Vortex-Surface Interactions", Proceedings of ASME Fluids Engineering Division Summer Meeting, Manuscript No. FEDSM 98-5720, June 21-25, 1998, Washington, D.C.

[28]Landreth, C. C. and Adrian, R. J., "Measurement and Refinement of Velocity Data Using High-Image-Density Analysis in Particle Image Velocimetry", Applications of Laser Anemometry to Fluid Mechanics (eds., R. Adrian, T. Asanuma, D. Durão, F. Durst, and J. Whitelaw), Springer-Verlag, NY, 1989, pp. 484-497.

[29]Liu, Z.-C., Landreth, C. C., Adrian, R. J. and Hanratty, T. J., "High Resolution Measurement of Turbulent Structure in a Channel with particle Image Velocimetry", *Experiments in Fluids*, Vol. 10, 1991, pp. 301-312.

[30]Westerweel, J., Draad, A. A., van der Hoevern, J. G. Th. and van Oord, J., "Measurement of Fully-Developed Turbulent Pipe Flow with Digital Particle Image Velocimetry", *Experiments in Fluids*, Vol. 20, 1996, pp. 165-177.

[31]Klebanoff, P. S., "Characteristics of Turbulence in a Boundary Layer with Zero Pressure Gradient", NACA Report 1247, 1995.

[32]Schlichting, H., Boundary-Layer Theory (7th Edition), McGraw-Hill Book Company, NY, 1979, p. 567.

[33]Bradshaw, P., An Introduction to Turbulence and Its Measurement, Pergaman Press, NY, 1971.

[34]Landreth, C. C. and Adrian, R. J., "Impingement of a Low Reynolds Number Turbulent Circular Jet onto a Flat Plate at Normal Incidence", *Experiments in Fluids*, Vol. 9, 1990, pp. 74-84.

[35]Fiedler, H. E., Dziomba, B., Mensing, P. and Rösgen, T., "Initiation, Evolution, and Global Consequences of Coherent Structures in Turbulent Shear Flows", Lecture Notes in Physics, Vol. 136, Springer-Verlag, 1981, pp. 219-251.

[36]Hussain, A. K. M. F., "Coherent Structures and Studies of Perturbed and Unperturbed Jets", Role for Coherent Structures in Modelling Turbulence and Mixing (ed. J. Jimenez), Lecture Notes in Physics, No. 136, Springer Verlag, pp. 252-291.

X. List of Figures

Figure 1: Principle elements of self-sustaining oscillations of turbulent flow past a cavity.

Figure 2: Overview of cavity test section located within main test section of water channel.

Figure 3: Representative image of instantaneous velocity field of turbulent boundary layer viewed in a reference frame moving at 0.8 U_∞; and variation of the mean $\overline{u}$ and fluctuating u_{rms} and v_{rms} velocities and the velocity correlation $-\overline{u'v'}$ across the boundary layer, all normalized by the freestream velocity U_∞.

Figure 4: Spectra of velocity fluctuations in the turbulent boundary layer, as obtained from PIV data. The spectra were evaluated at a distance of 0.91 inches from the wall corresponding to 0.5δ, where $\delta = \delta_{995}$ is the boundary layer thickness.

Figure 5: Time trace of pressure at impingement corner acquired simultaneously with the cinema PIV series. The framing rate of the cinema sequence is ten frames/sec and the first image of cinema sequence corresponds to $t = 0.1$ sec in the trace of pressure. Subsequent images correspond to $t = 0.2$, 0.3 sec and so on in pressure trace.

Figure 6a: Instantaneous distributions of velocity and vorticity during cavity oscillation in a mode corresponding approximately to the fundamental frequency β of the cavity shear layer. At the instant shown, the pressure at the corner has its maximum negative value.

Figure 6b: Instantaneous distributions of velocity and vorticity during cavity oscillation in a mode corresponding approximately to the fundamental frequency β of the cavity shear layer. At the instant shown, the pressure at the corner has its maximum negative value. The velocity field is shown in reference frames moving at 0.25 and 0.50 U_∞, in which U_∞ is the freestream velocity.

Figure 7: Instantaneous distributions of velocity and vorticity during cavity oscillation in a mode corresponding approximately to the fundamental frequency β of the cavity shear layer. At the instant shown, the pressure at the corner has its maximum positive value.

Figure 8: Instantaneous distributions of velocity and vorticity during cavity oscillation in a mode corresponding approximately to the subharmonic frequency $\beta/2$ of the most amplified component β of the cavity shear layer. At the instant shown, the pressure at the corner has its maximum negative value. (Images represent transformed version of those of Lin and Rockwell[27]).

Figure 9: Instantaneous distributions of velocity and vorticity during cavity oscillation in a mode corresponding approximately to the subharmonic frequency $\beta/2$ of the most amplified, fundamental component β of the cavity shear layer. At the instant shown, the pressure at the corner has its maximum positive value.

Figure 10: Comparison of representative instantaneous velocity field in cavity [top image] with instantaneous velocity field calculated using a large-eddy simulation technique by Takakura et al. (1996) [bottom image]. For the calculated flow, the flow region exterior to the cavity is supersonic.

Figure 11: Comparison of representative instantaneous vorticity distribution in the oscillating shear layer [top image] with the instantaneous vorticity distribution numerically calculated by Pereira and Sousa (1995) [bottom image]. For numerically-calculated images, solid lines are vorticity contours and dashed lines are instantaneous streamlines.

Figure 12: Distributions of averaged velocity $< V >$ based on cinema sequence [top image] and randomly-acquired sequence [bottom image].

Figure 13: Contours of constant averaged vorticity $< \omega >$ corresponding to cinema sequence [top image] and randomly-acquired sequence [bottom image] of PIV images. Minimum positive and negative contour levels correspond to ± 2 sec^{-1} and incremental level to 2 sec^{-1}.

Figure 14: Contours of constant Reynolds stress normalized by the free-stream velocity $< u'v' > / U_\infty^2$ for cinema sequence [top image] and randomly-acquired sequence [bottom image] of PIV images. Minimum contour level corresponds to 0.0005 and incremental level is 0.0005.

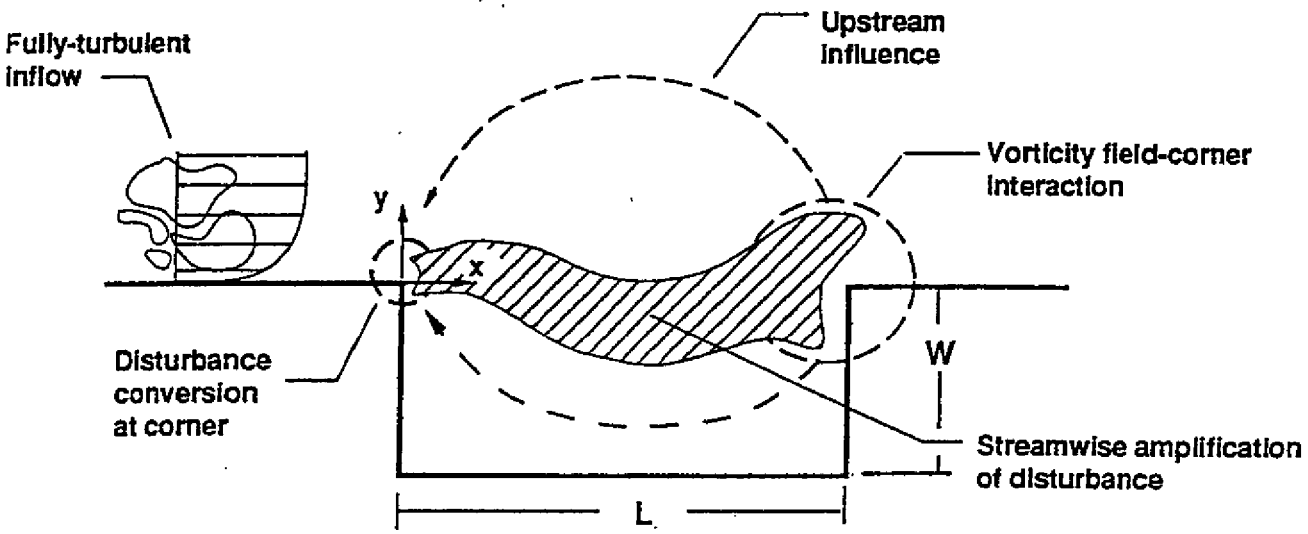

Figure 1: Principal elements of self-sustaining oscillations of turbulent flow past a cavity.

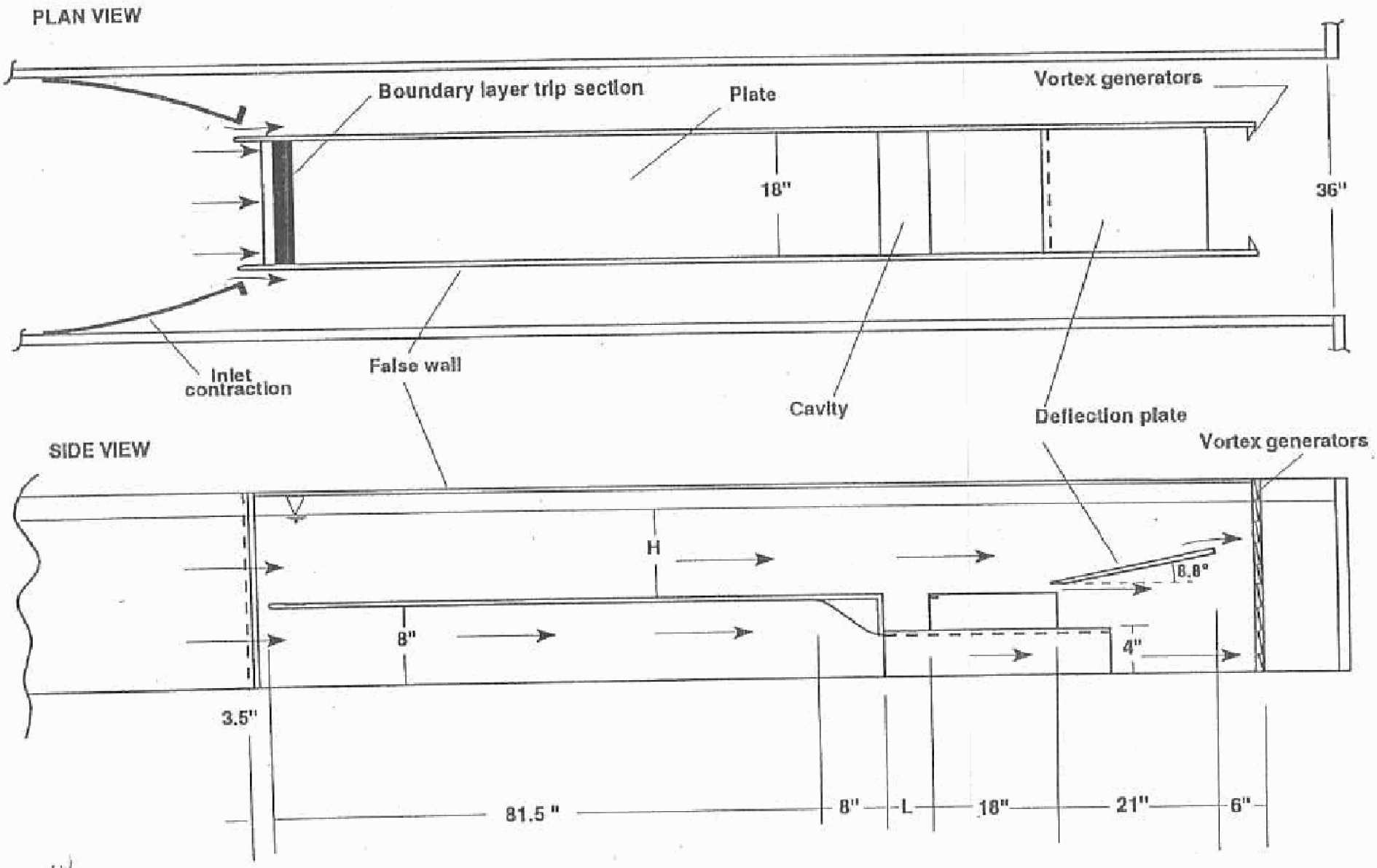

Figure 2: Overview of cavity test section located within main test section of water channel.

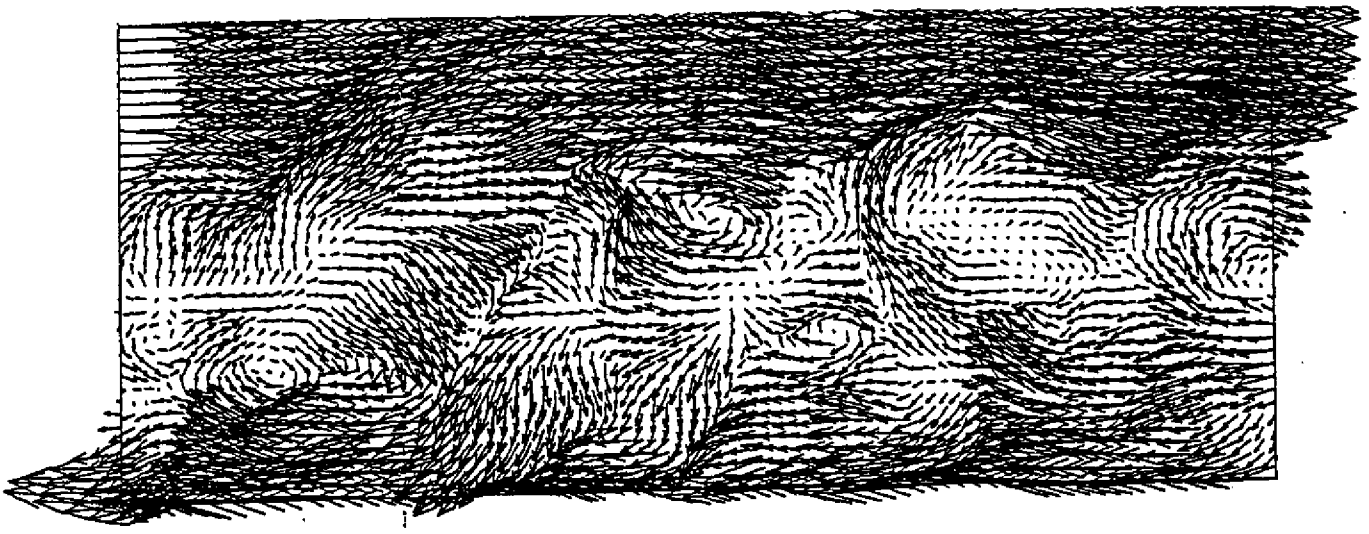

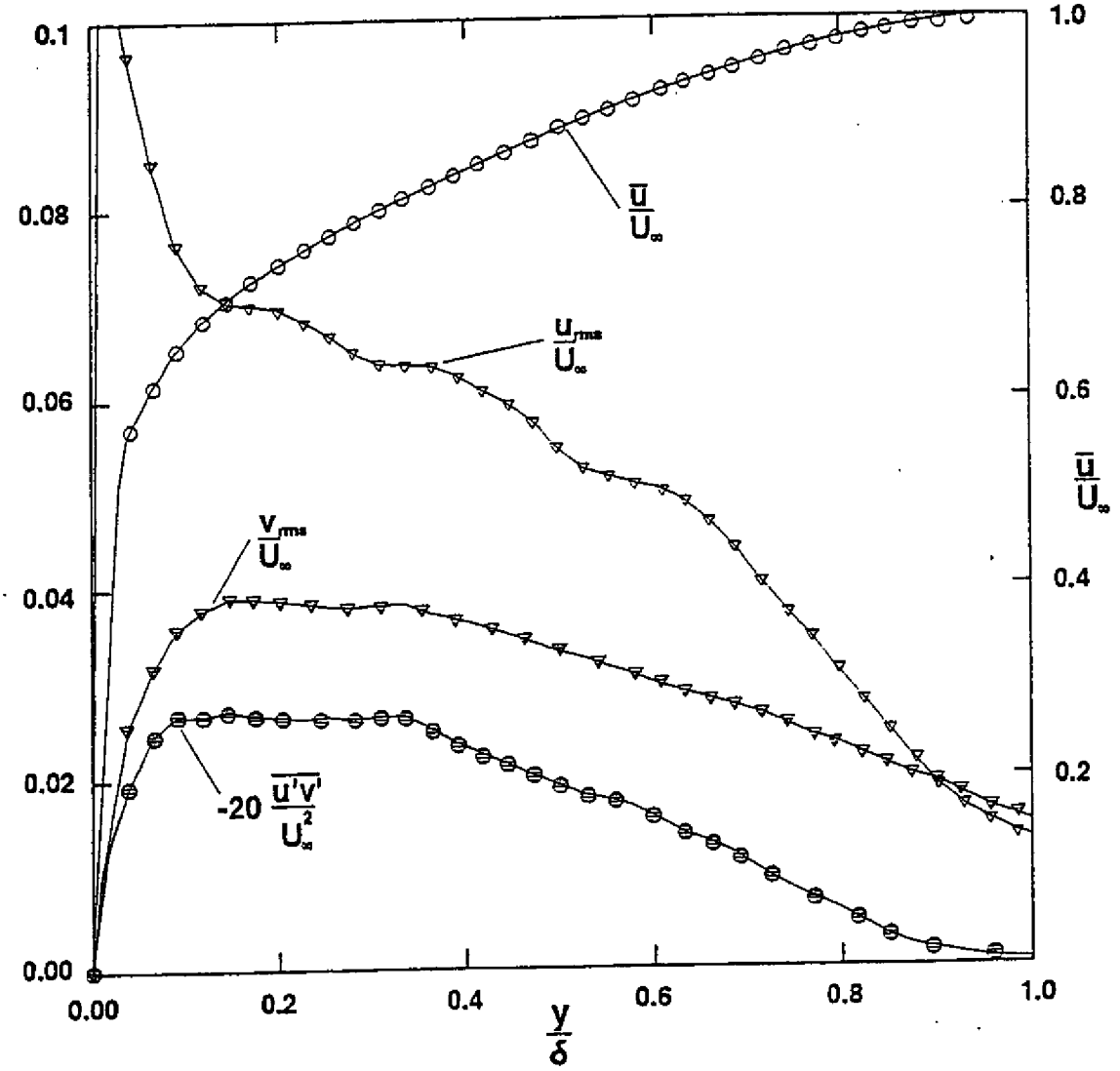

Figure 3: Representative image of instantaneous velocity field of turbulent boundary layer viewed in a reference frame moving at 0.8 U_∞; and variation of the mean $\bar{u}$ and fluctuating u_{rms} and v_{rms} velocities and

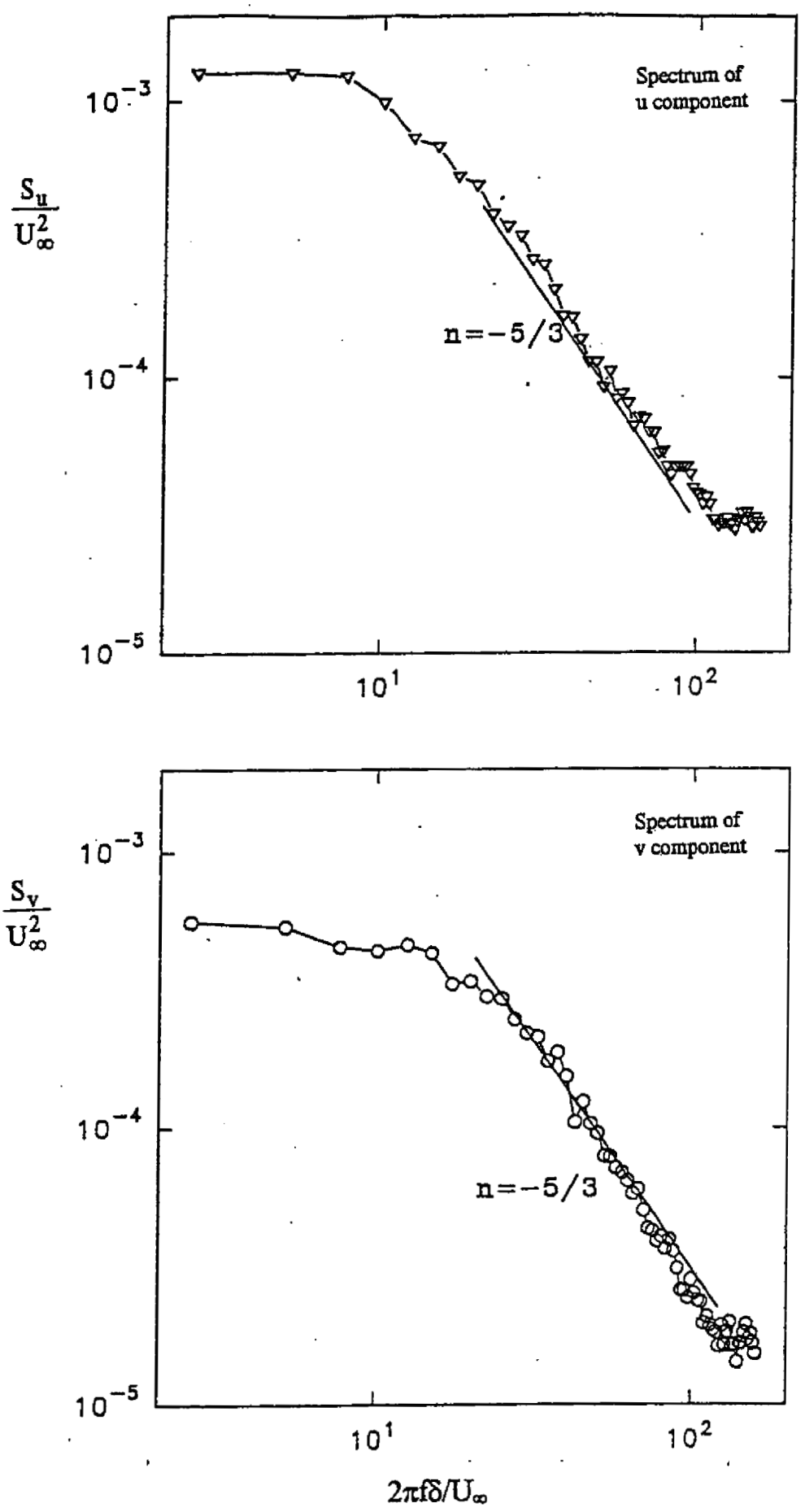

Figure 4: Spectra of velocity fluctuations in the turbulent boundary layer, as obtained from PIV data. The

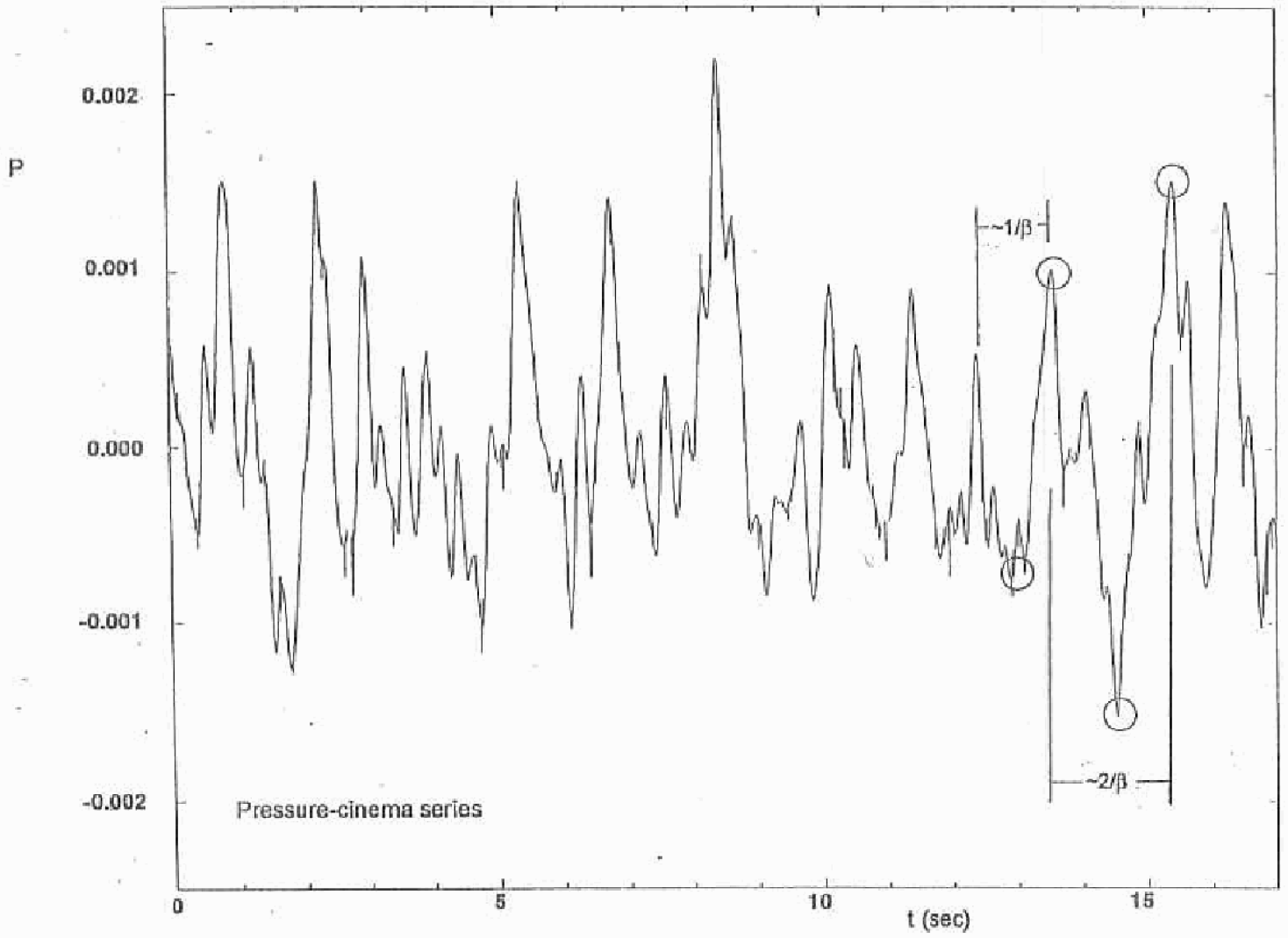

Figure 5: Time trace of pressure at impingement corner acquired simultaneously with the cinema PIV series. The framing rate of the cinema sequence is ten frames/sec and the first image of cinema sequence corresponds to t = 0.1 sec in the trace of pressure. Subsequent images correspond to t = 0.2, 0.3 sec and so on in pressure trace.

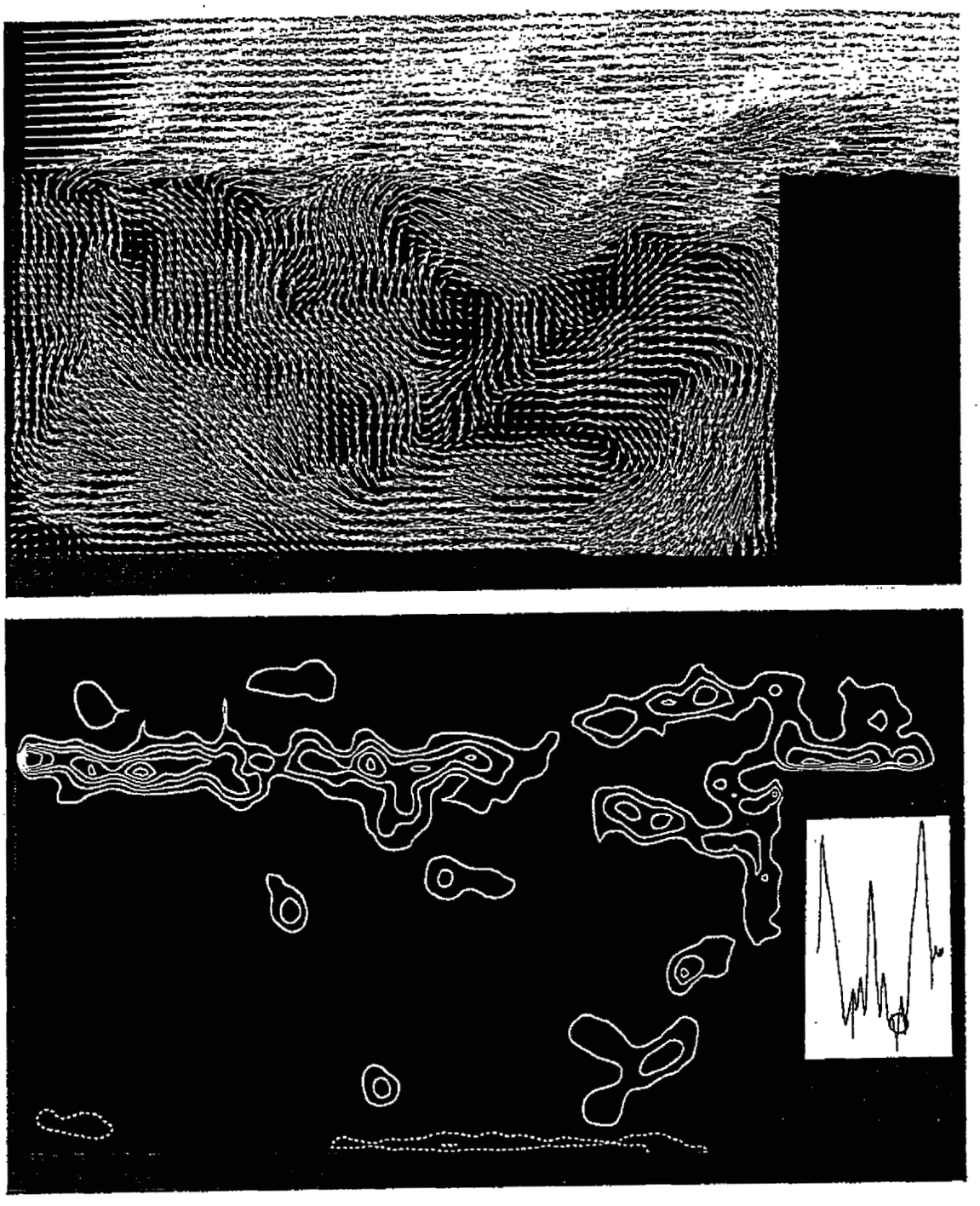

Figure 6a: Instantaneous distributions of velocity and vorticity during cavity oscillation in a mode corresponding approximately to the fundamental frequency β of the cavity shear layer. At the instant shown, the pressure at the corner has its maximum negative value.

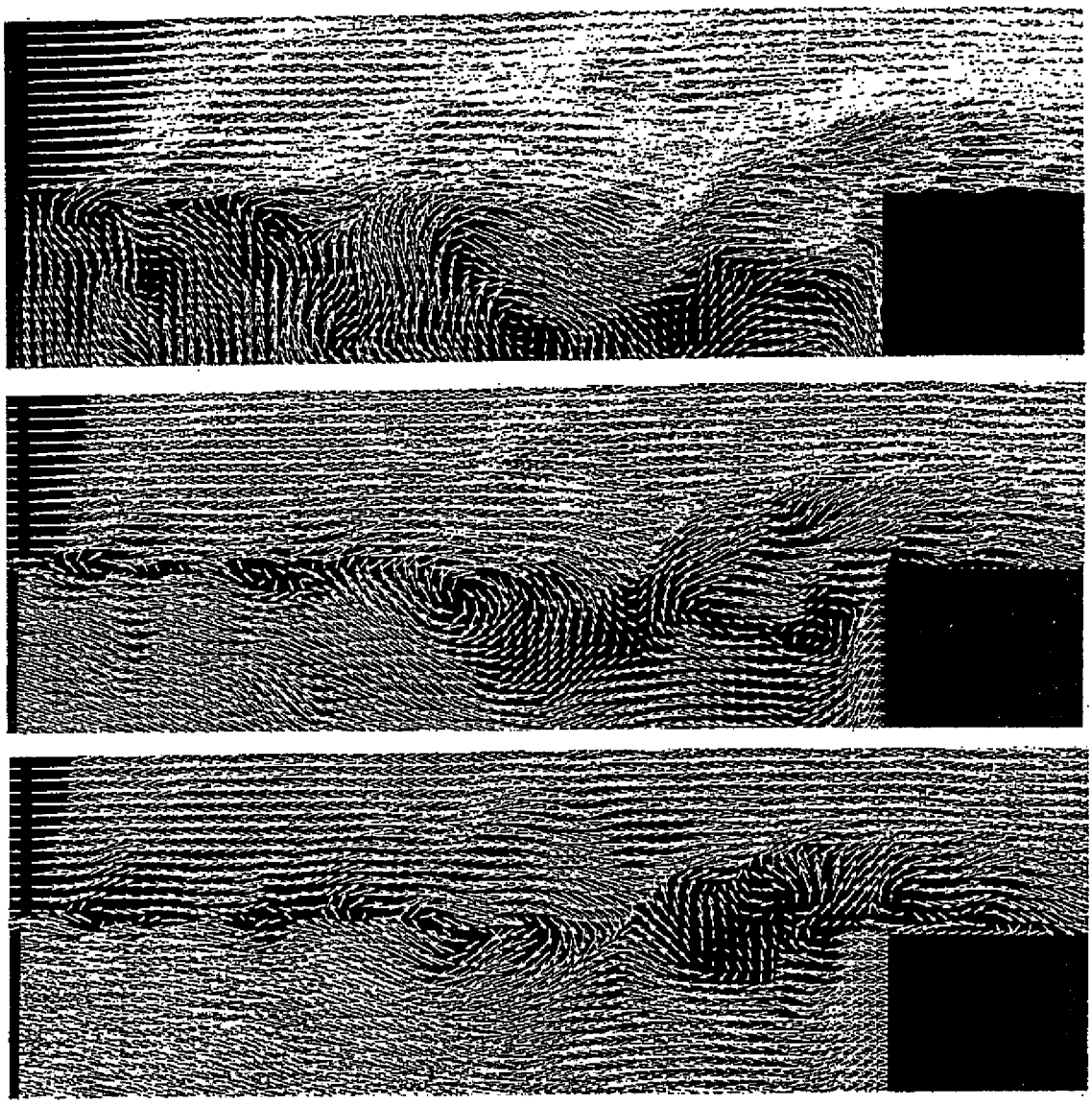

Figure 6b: Instantaneous distributions of velocity and vorticity during cavity oscillation in a mode corresponding approximately to the fundamental frequency β of the cavity shear layer. At the instant shown, the pressure at the corner has its maximum negative value. The velocity field is shown in reference frames moving at 0.25 and 0.50 U_∞, in which U_∞ is the freestream velocity.

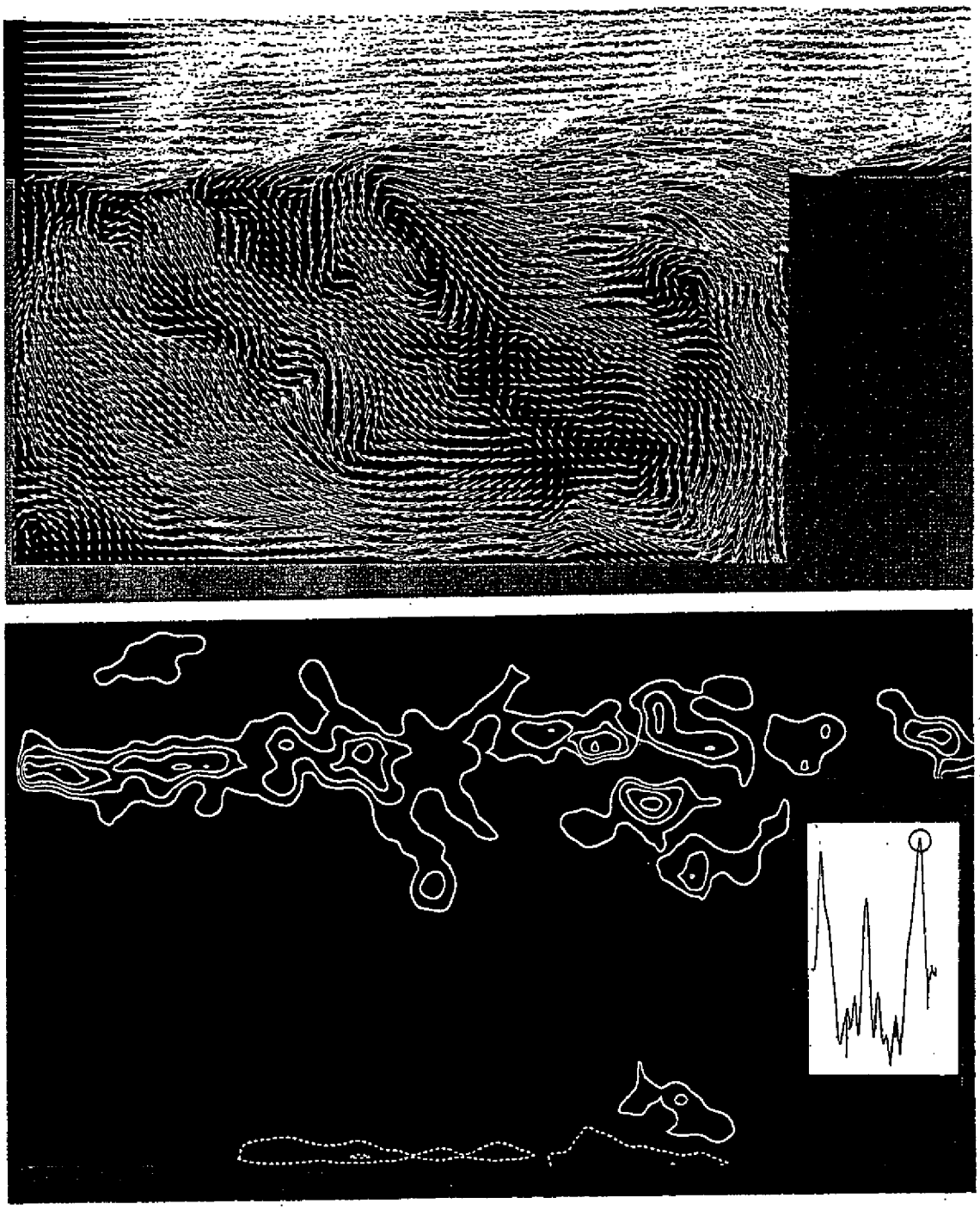

Figure 7: Instantaneous distributions of velocity and vorticity during cavity oscillation in a mode corresponding approximately to the fundamental frequency β of the cavity shear layer. At the instant shown, the pressure at the corner has its maximum positive value.

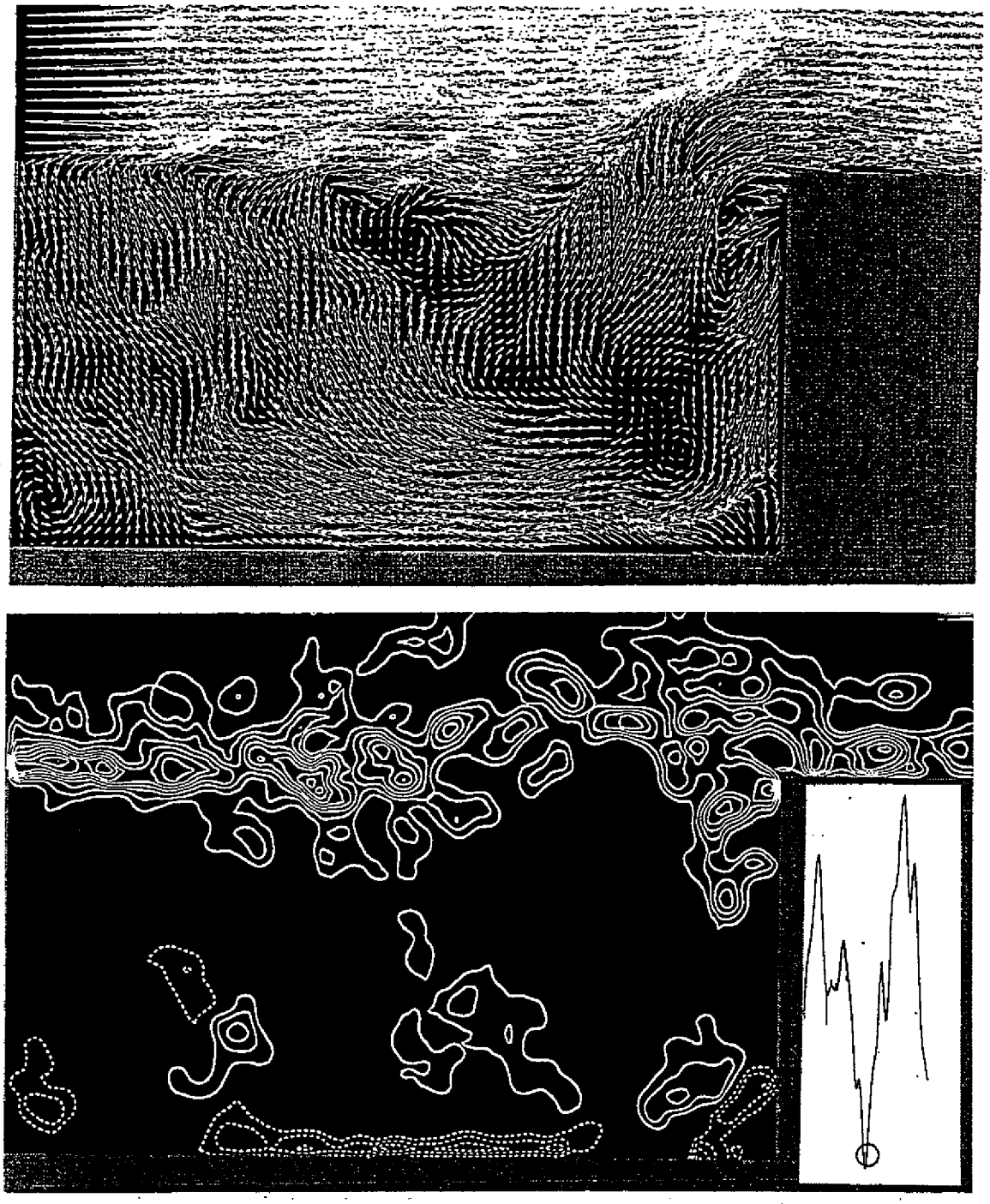

Figure 8: Instantaneous distributions of velocity and vorticity during cavity oscillation in a mode corresponding approximately to the subharmonic frequency $\beta/2$ of the most amplified component β of the cavity shear layer. At the instant shown, the pressure at the corner has its maximum negative value. (Images represent transformed version of those of Lin and Rockwell[27]).

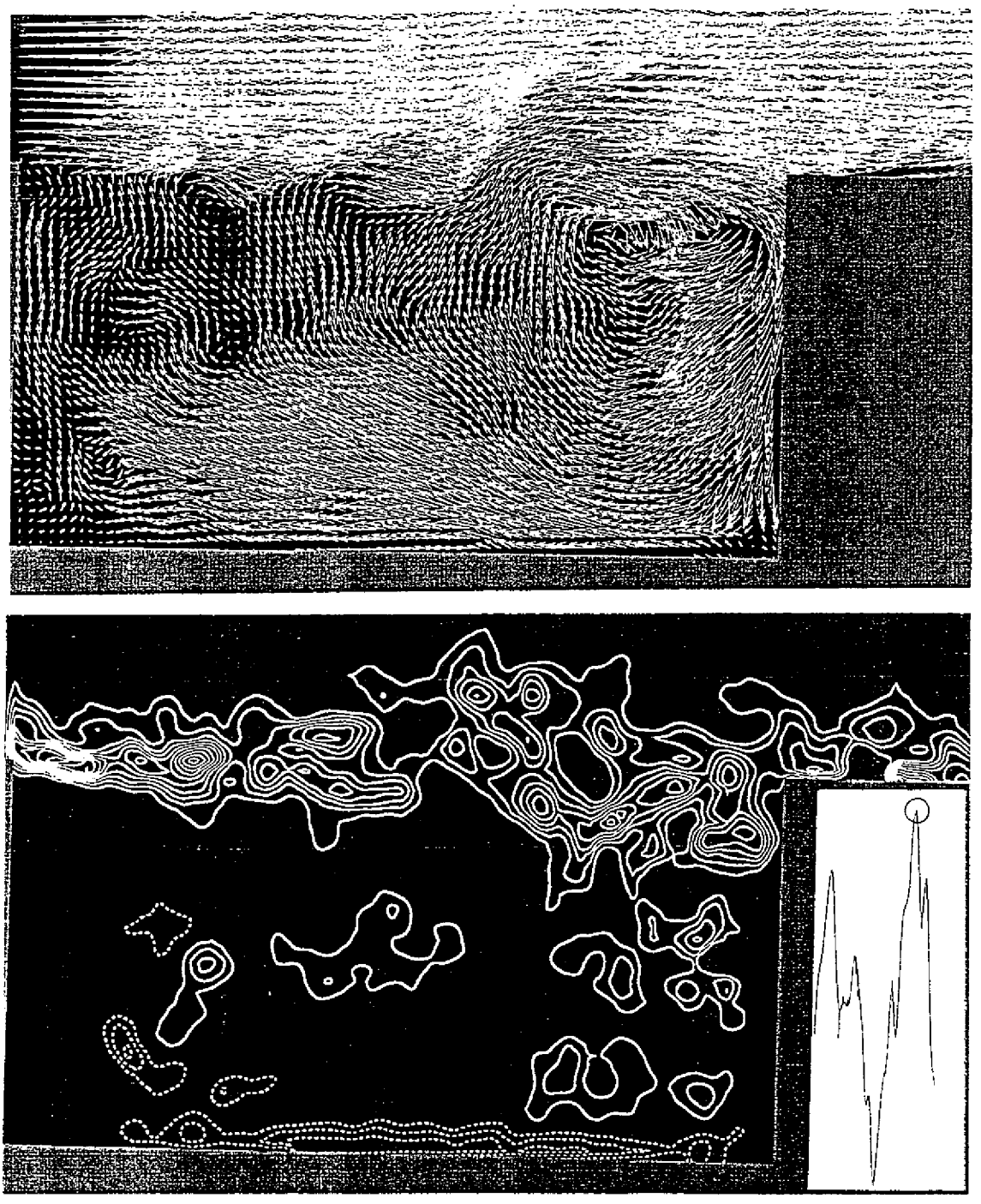

Figure 9: Instantaneous distributions of velocity and vorticity during cavity oscillation in a mode corresponding approximately to the subharmonic frequency $\beta/2$ of the most amplified, fundamental component β of the cavity shear layer. At the instant shown, the pressure at the corner has its maximum positive value.

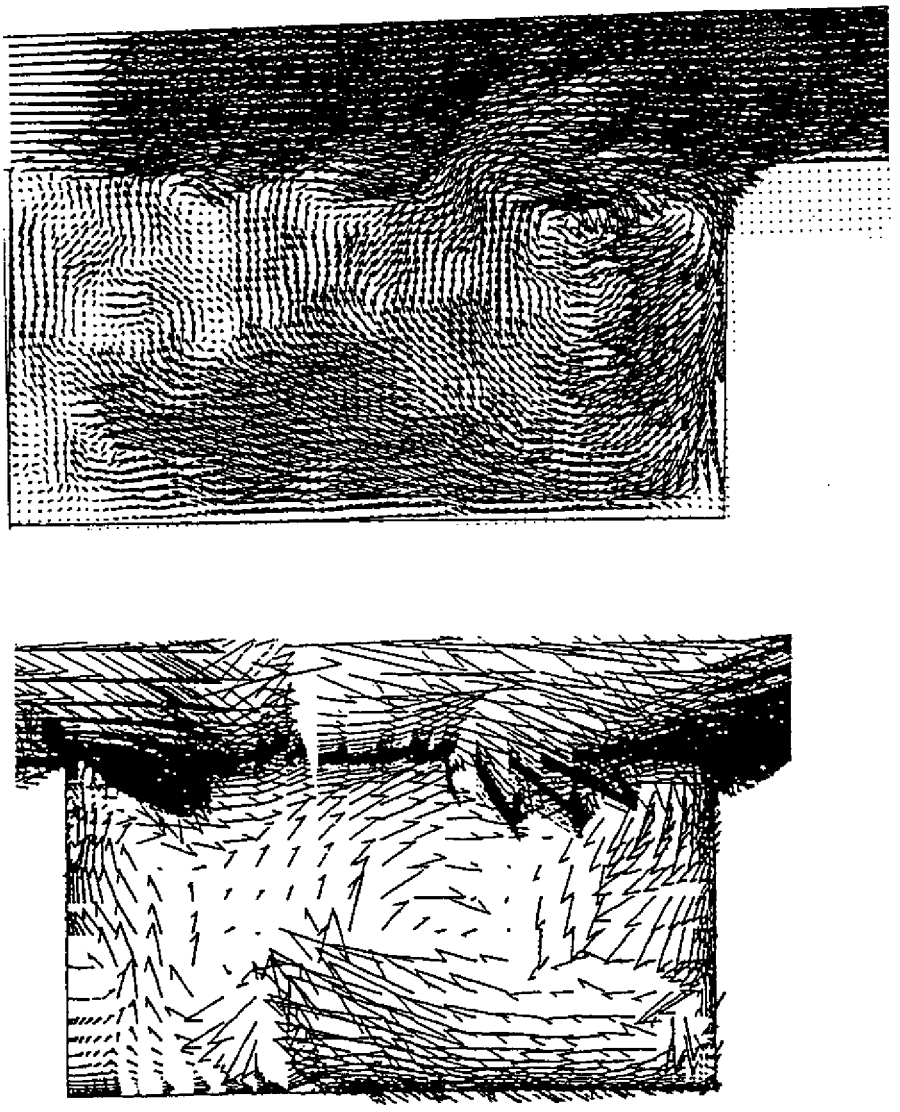

Figure 10: Comparison of representative instantaneous velocity field in cavity [top image] with instantaneous velocity field calculated using a large-eddy simulation technique by Takakura et al. (1996) [bottom image]. For the calculated flow, the flow region exterior to the cavity is supersonic.

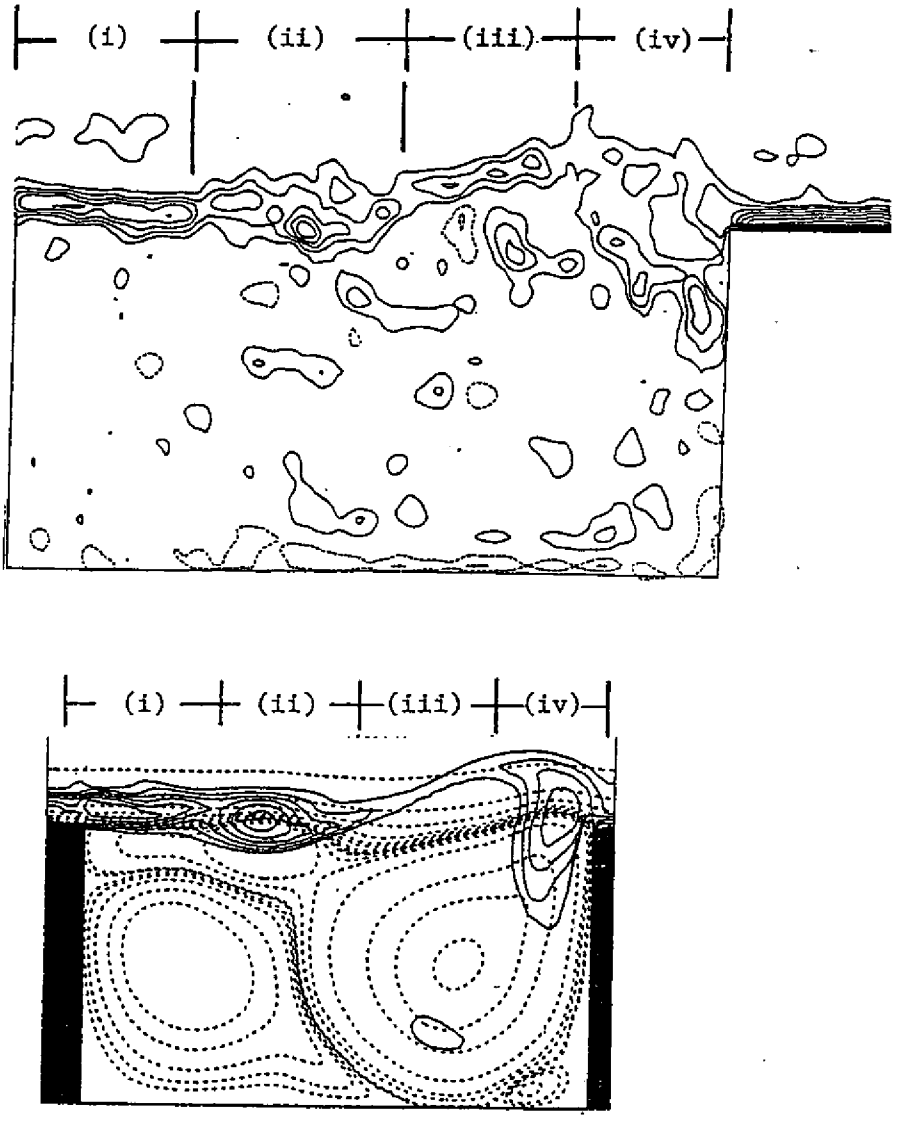

Figure 11: Comparison of representative instantaneous vorticity distribution in the oscillating shear layer [top image] with the instantaneous vorticity distribution numerically calculated by Pereira and Sousa (1995) [bottom image]. For numerically-calculated images, solid lines are vorticity contours and dashed lines are instantaneous streamlines.

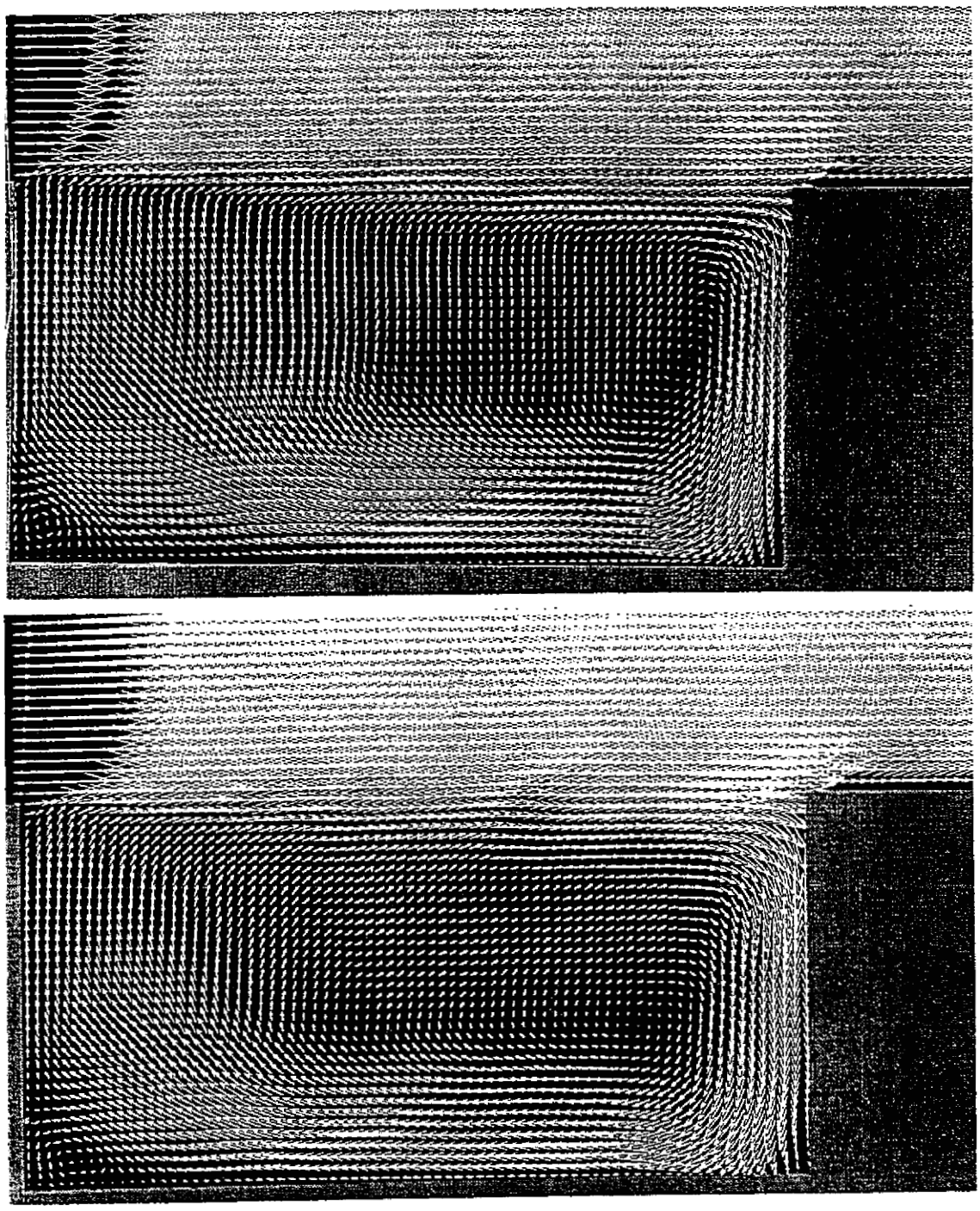

Figure 12: Distributions of averaged velocity $< V >$ based on cinema sequence [top image] and randomly-acquired sequence [bottom image].

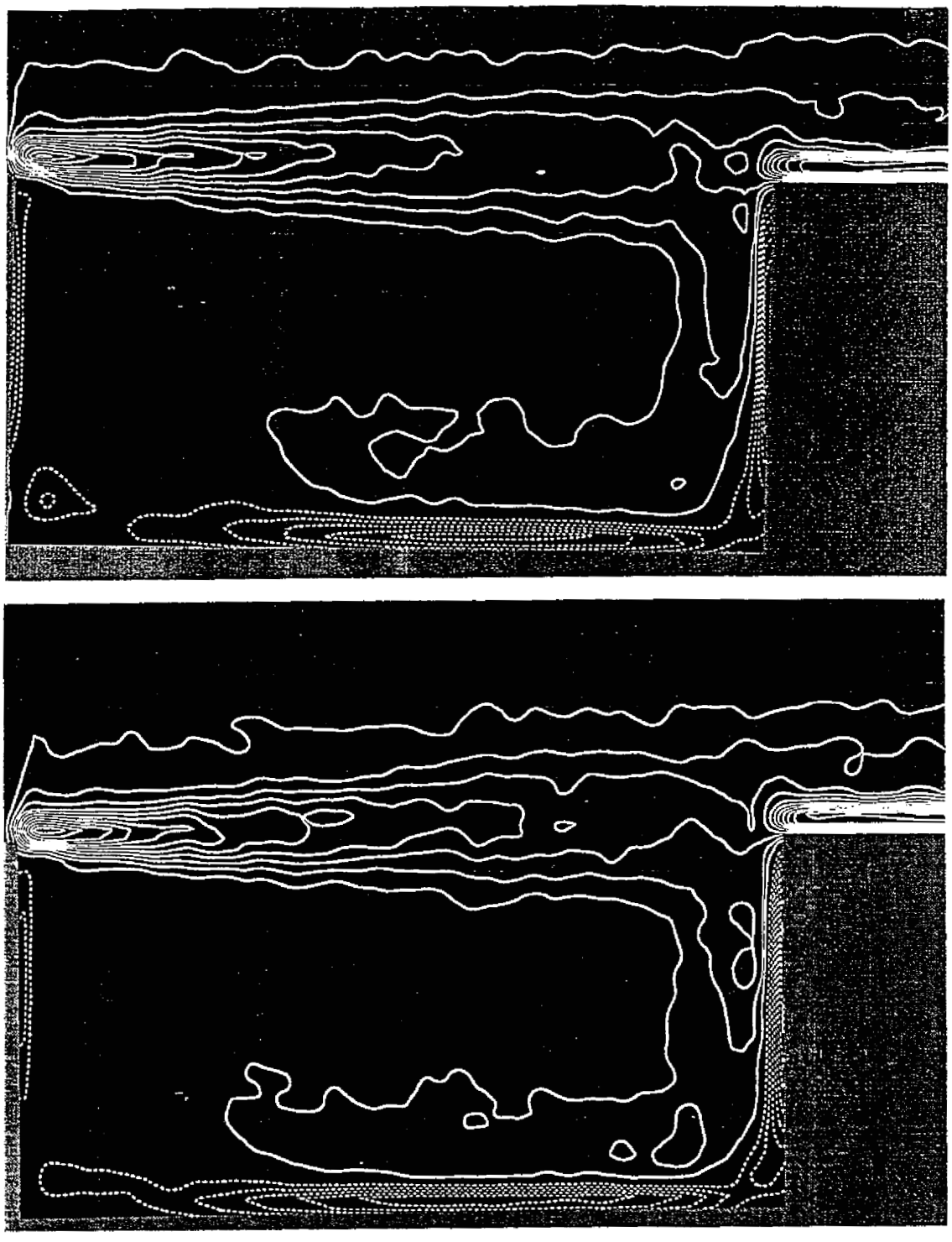

Figure 13: Contours of constant averaged vorticity $< \omega >$ corresponding to cinema sequence [top image] and randomly-acquired sequence [bottom image] of PIV images. Minimum positive and negative contour levels correspond to ± 2 sec^{-1} and incremental level to 2 sec^{-1}.

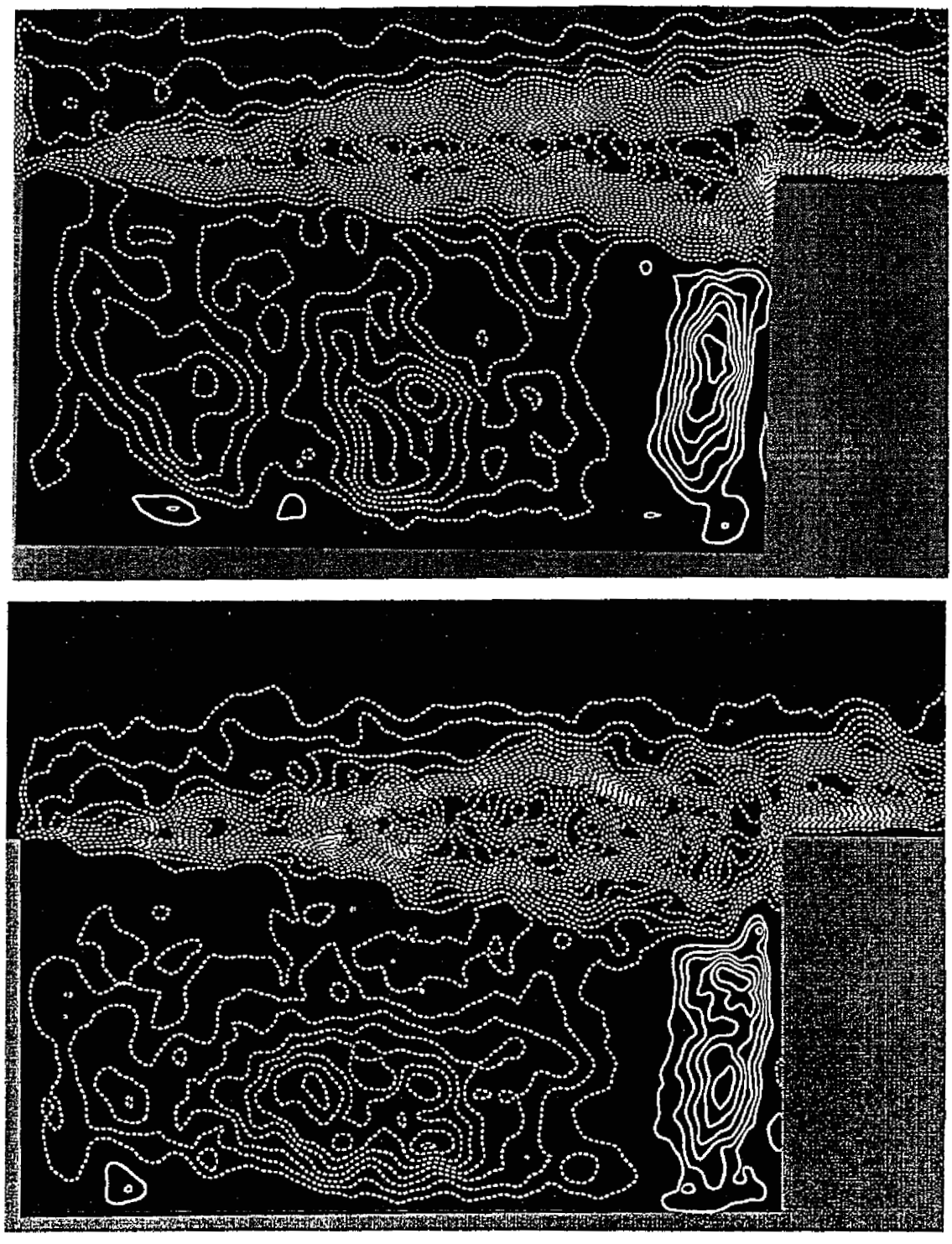

Figure 14: Contours of constant Reynolds stress normalized by the free-stream velocity $< u'v' > / U_\infty^2$ for cinema sequence [top image] and randomly-acquired sequence [bottom image] of PIV images. Minimum contour level corresponds to 0.0005 and incremental level is 0.0005.